https://doi.org/10.5194/egusphere-2026-6588
Preprint. Discussion started: 22 November 2026
© Author(s) 2026. CC BY 4.0 License.

Loss, recovery and hysteresis of polar sea ice in TIPMIP multi-model simulations

Tian Tian[1], Shuting Yang[1], Oliver Tooth[2], Colin Jones[3], Torben Koenigk[4,5], Thomas L. Frölicher[6,7], Thomas Torsvik[8], Mehdi Pasha Karami[4], Chuncheng Guo[1], Nicole C. Laureanti[9,10], Rashed Mahmood[1], Manabu Abe[11], Pascale Braconnot[12], Patricia Cadule[13], Frederic Castruccio[14], Gokhan Danabasoglu[14], Urs Hofmann Elizondo[6], Friederike Fröb[8], Nicolas M. Leitmann-Niimi[15], Paul Lerner[15], Anastasia Romanou[15,16], Roland Séférian[17], Tokuta Yokohata[18], and Tilo Ziehn[19]

[1]Danish Meteorological Institute, Copenhagen, Denmark
[2]National Oceanography Centre, Southampton, UK
[3]National Centre for Atmospheric Science, University of Leeds, Leeds, UK
[4]Swedish Meteorological and Hydrological Institute, Norrköping, Sweden
[5]Bolin Centre for Climate Research, Stockholm University, Stockholm, Sweden
[6]Climate and Environmental Physics, University of Bern, Bern, Switzerland
[7]Oeschger Centre for Climate Change Research, University of Bern, Bern, Switzerland
[8]Geophysical Institute, University of Bergen and Bjerknes Centre for Climate Research, Bergen, Norway
[9]Potsdam Institute for Climate Impact Research, Member of the Leibniz Association, Potsdam, Germany
[10]Max Planck Institute for Geoanthropology, Jena, Germany
[11]Research Institute for Global Change, Japan Agency for Marine-Earth Science and Technology, Yokohama, Japan
[12]Laboratoire des Sciences du Climat et de l'Environnement, Institut Pierre-Simon Laplace, CNRS, CEA, Université de Versailles Saint-Quentin-en-Yvelines, Université Paris-Saclay, Gif-sur-Yvette, France
[13]LMD-IPSL, CNRS, Ecole normale supérieure/PSL, Sorbonne Université, Ecole Polytechnique, Paris, France
[14]US National Science Foundation National Center for Atmospheric Research, Boulder, USA
[15]Department of Applied Physics and Applied Mathematics, Columbia University, New York, USA
[16]NASA Goddard Institute for Space Studies, New York, USA
[17]CNRM, Université de Toulouse, Météo-France, CNRS, Toulouse, France
[18]Earth System Division, National Institute for Environmental Studies, Tsukuba, Japan
[19]CSIRO Environment, Aspendale, Australia

Correspondence: Tian Tian (tian@dmi.dk)

Abstract. Polar sea ice may not recover to the same mean state after a temperature overshoot, even when global mean temperature returns to the pre-overshoot level. Yet, multi-model evidence for polar sea ice reversibility remains limited. Here we analyse Tier-1 simulations from ten Earth system models (ESMs) participating in the Tipping Points Modelling Intercomparison Project (TIPMIP) to assess sea ice stability, reversibility and global warming pathway dependence across constant positive CO_2-emission (warming), zero-emission, constant negative CO_2-emission (cooling) and post-overshoot pathways. Winter polar amplification provides the thermal context for sea ice change: Arctic amplification is strong but generally weakens at higher global warming levels (GWLs), whereas Antarctic polar amplification increases more strongly with warming and remains elevated following overshoot in most models. Stronger winter Arctic amplification is generally associated with earlier Arctic summer ice-free onset, but its onset spans a wide range of GWLs, indicating no common threshold across models. Different sea ice states can also occur at similar GWLs. Arctic hysteresis is weak in most models, although a few models exhibit over-

https://doi.org/10.5194/egusphere-2026-6588
Preprint. Discussion started: 22 November 2026
© Author(s) 2026. CC BY 4.0 License.

recovery. This over-recovery broadly coincides with AMOC weakening and reduced poleward ocean heat transport reported in a companion multi-model ocean analysis. This association is strongest in GISS-E2-1-G-CC2, where the largest Arctic cooling and sea ice expansion occur alongside incomplete AMOC recovery, while other models show delayed AMOC recovery. Antarctic sea ice shows more robust delayed recovery during cooling from 4°C GWL, particularly in sea ice mass. Thermodynamic mass-budget diagnostics from four models show different combinations of basal and frazil growth and basal and surface melt at 2°C GWL, depending on whether the system arrives directly from warming or after following an overshoot-cooling pathway. These results show that GWL alone is insufficient to infer polar sea ice reversibility and that overshoot can leave persistent thermal and thermodynamic signatures on the sea ice system.

1 Introduction

Sea ice is one of the most visible and dynamically important components of polar climate change. Its decline alters surface albedo, ocean-atmosphere heat and carbon exchange, and freshwater fluxes, with consequences for marine ecosystems, while ice-albedo and surface-flux feedbacks further enhance regional climate change (Serreze and Barry, 2011; Screen and Simmonds, 2010b). Future sea ice loss is expected in both hemispheres, but the Coupled Model Intercomparison Project Phase 6 (CMIP6) projections show substantial inter-model spread, with large differences in the timing, magnitude and spatial pattern in the Arctic and particularly low confidence in the Antarctic winter sea ice change (Notz and SIMIP Community, 2020; Keen et al., 2021; Roach et al., 2020; Holmes et al., 2022). This spread arises from a combination of internal climate variability and structural differences among models, including differences in their climate sensitivity to CO_2 forcing (Zelinka et al., 2020; Ye and Messori, 2021; Li et al., 2025; Yu et al., 2025). Differences in polar temperature responses, ocean-atmosphere processes and the representation of sea ice growth and melt further contribute to contrasting sea ice evolution across models (Keen et al., 2021; Zhang et al., 2023).

Keen et al. (2021) provided a process-based perspective, finding that Arctic sea ice production is dominated by basal and frazil growth, whereas thermodynamic loss is dominated by basal and surface melt. The overall structure of the sea ice mass budget is similar across CMIP6 models, but the magnitude and evolution of individual budget components vary considerably and are strongly dependent on the changing ice state. Process-level evaluation against ice mass balance buoy observations further shows that CMIP6 models tend to overestimate sea ice growth, melt and conductive heat fluxes, while substantial inter-model differences remain in the magnitude and the seasonal cycle of these fluxes, suggesting structural uncertainty in the representation of sea ice thermodynamics (West and Blockley, 2025).

Recent CMIP6 analyses also indicate that sea ice is one of the climate-system components that can exhibit strong nonlinear responses and abrupt state transitions under future warming (Romanou et al., 2023; Angevaare and Drijfhout, 2026; Wu et al., 2026). However, conventional transient warming scenarios are limited in what they can tell us about reversibility (Armour

https://doi.org/10.5194/egusphere-2026-6588
Preprint. Discussion started: 22 November 2026
© Author(s) 2026. CC BY 4.0 License.

et al., 2011). They show how sea ice is lost as forcing increases but cannot be used to explore whether sea ice stabilises when global temperature is held approximately constant, or whether the same ice state is recovered when temperatures subsequently cool, or whether the physical processes governing sea ice changes differ between warming and cooling (Smith et al., 2026). These questions are particularly important for overshoot scenarios in which the global mean temperature reverts back to a previous level while regional polar temperatures, ocean heat content and sea ice conditions may still carry the imprint of the previous warming history (Roldán-Gómez et al., 2025). In CMIP6 overshoot simulations, changes during the warming phase are not necessarily compensated during subsequent cooling, with sea ice and meridional overturning changes contributing to persistent regional temperature asymmetries (Schwinger et al., 2022; Lacroix et al., 2024; Roldán-Gómez et al., 2025).

The thermal context for sea ice change is also highly seasonal and hemisphere-asymmetric. Polar amplification (PA) differs between the Arctic and Antarctic, exhibiting a strong seasonal structure in CMIP6 projections (Xie et al., 2022; Zhang et al., 2023). Arctic winter amplification is a robust feature across models despite substantial variation in magnitude, whereas Antarctic amplification is generally weaker, more heterogeneous and more sensitive to forcing level and model-specific ocean-atmosphere coupling (Xie et al., 2022; Ye and Messori, 2021; Zhang et al., 2023; Linke et al., 2026). At the same time, polar winter processes have received less attention than summer sea ice loss, despite their importance for sea ice growth, ocean-atmosphere exchange and high-latitude climate feedbacks (Screen and Simmonds, 2010a; Yang et al., 2026). This motivates our focus on winter PA when interpreting winter sea ice area and mass.

The TIPMIP Earth system model (ESM) Tier-1 experiments (Jones et al., 2026; Winkelmann et al., 2025), hereafter referred to as Tier-1, provide a controlled framework for addressing these questions. All experiments are run in CO_2-emission mode, with atmospheric CO_2 therefore evolving interactively as a model-predicted variable. Their positive CO_2-emission (warming), zero-emission, negative CO_2-emission (cooling), and post-overshoot (zero-emission) pathways allow sea ice states to be compared between models at similar rates and levels of global warming and cooling (Smith et al., 2026, Table 1). Sea ice loss during warming is characterised using the positive-emission experiment; adjustment under zero emissions at 2 and 4°C GWLs is examined using ZE-2 and ZE-4; reversibility during cooling is assessed using Dn2 and Dn4; and Dn4-ZE-2 is used to test whether a return to 2°C after a 4°C overshoot leads to the same sea ice state as the direct ZE-2 pathway. Together, these experiments allow direct assessment of pathway dependence, immediate or delayed recovery, and hysteresis, with participating models approximately following common global warming, stabilisation, and global cooling pathways.

We analyse Arctic and Antarctic sea ice responses from ten ESMs that contributed to the Tier-1 experiments. We first investigate pathway-dependent polar temperature responses and winter PA and their relationship with the timing of Arctic summer ice-free onset. We then evaluate sea ice loss, zero-emission adjustment, and overshoot recovery using sea ice area, mass, and spatial sea ice concentration diagnostics. Reversibility is quantified by comparing the cooling and warming branches at matched GWLs to diagnose sea ice hysteresis. Finally, we examine basal growth, frazil ice formation, basal melt, and surface melt for the four models with available thermodynamic mass-budget diagnostics to identify processes associated with delayed recovery, over-recovery, and pathway memory. Together, these analyses test how polar sea ice states and thermodynamic balances depend on both the amount of warming and the climate pathway through which that warming level is reached, and how these responses vary across models.

https://doi.org/10.5194/egusphere-2026-6588
Preprint. Discussion started: 22 November 2026
© Author(s) 2026. CC BY 4.0 License.

2 Data and methods

2.1 Tier-1 experiments and model ensemble

The Tier-1 protocol is described in Jones et al. (2026) and Winkelmann et al. (2025). The protocol requires ESMs to run in CO_2-emission mode. It starts with an idealised CO_2-emission pathway designed to produce an approximately common global mean surface air temperature (GMSAT) warming rate of 2°C per century across models. The positive-emission experiment (i.e., ramp-up, hereafter referred to as UPs) provides the warming branch from which the remaining experiments are initiated (Fig. S1).

The zero-emission experiments, ZE-2 and ZE-4, branch from UPs when GMSAT reaches 2 and 4°C above the pre-industrial (PI) reference, respectively, with the prescribed CO_2 emissions set to zero. The negative-emission (i.e., ramp-down) experiments, Dn2 and Dn4, are initiated after 50 years of the corresponding zero-emission experiments but using the same rate as during UPs. Dn4-ZE-2 is branched from Dn4 when GMSAT returns to 2°C above PI, afterwards CO_2 emissions are again set to zero. This branching structure enables direct comparison of warming, zero-emission, cooling, and post-overshoot states within a common experimental framework. The experiments and terminology used throughout the manuscript are summarised in Table 1.

We analyse one ensemble member from each of the ten participating ESMs. All ten models are included in the temperature and sea ice state analyses. Ramp-down simulations are available for nine models, while four models provide a consistent set of thermodynamic sea ice mass-budget diagnostics used here: EC-Earth3-ESM-1, GISS-E2-1-G-CC2, NorESM2-LM, and UKESM1-2-LL. Model components and references are summarised in Table A1 and Appendix A.

As prescribed by the Tier-1 protocol, most models warm at close to 2°C per century during the ramp-up experiment, although not all reach 4°C within the nominal 200-year period (e.g., GISS-E2-1-G-CC2, CESM2, and IPSL-CM6-ESMCO2; Fig. S1a) as the transient climate response to cumulative carbon emissions (TCRE) is not strictly linear across warming levels and cumulative emissions. Some zero-emission branches, particularly ZE-4, retain residual warming after branching, with the largest positive GMSAT trends in NorESM2-LM, ACCESS-ESM1-5, and CESM2, and weaker positive trends in UKESM1-2-LL, GISS-E2-1-G-CC2, and GFDL-ESM2M (Fig. S1a). This is physically plausible because the transition from positive to zero CO_2 emissions is abrupt, whereas the climate system responds more gradually. At the lower warming level, ZE-2, two models instead show weak negative GMSAT trends. These deviations from the idealised pathway are accounted for in the model-specific analyses below.

2.2 Model output and sea ice diagnostics

For each model, the respective pre-industrial control simulation (PI-control, PI) is used to define the reference climate state. The PI climatology is calculated from 300 years of PI-control simulation, except NorESM2-LM for which there are only 250 years of data available. Anomalies are calculated relative to the corresponding model-specific PI climatology.

Monthly surface air temperature (SAT), sea ice concentration (SIC), sea ice area, and sea ice mass are analysed separately for the Arctic and Antarctic. Seasonal means are calculated for March–May (MAM), June–August (JJA), September–November

https://doi.org/10.5194/egusphere-2026-6588
Preprint. Discussion started: 22 November 2026
© Author(s) 2026. CC BY 4.0 License.

Table 1. TIPMIP ESM Tier-1 experiments, their prescribed pathway names, short names, and analytical purpose.

Experiment name in this paper	Prescribed pathway	Short names	Purpose in this study
PI	Pre-industrial control	PI-control	Reference climate and sea ice state
UPs	Positive CO_2 emissions	Ramp-up	Sea ice loss during progressive warming
ZE-2	Zero emissions after GWL=2°C	ZE-2 stabilised	Sea ice adjustment under zero emissions near 2°C GWL
Dn2	Negative CO_2 emissions from GWL=2°C	Dn2 / ramp-down	Sea ice recovery during cooling from 2°C GWL
ZE-4	Zero emissions after GWL=4°C	ZE-4 stabilised	Sea ice adjustment under zero emissions near 4°C GWL
Dn4	Negative CO_2 emissions from GWL=4°C	Dn4 / ramp-down	Sea ice recovery during cooling from 4°C GWL
Dn4-ZE-2	Zero emissions after cooling from 4°C toward 2°C GWL	Post-overshoot ZE-2	Assess the impact of a 4°C overshoot by comparing the post-overshoot 2°C sea ice state with the direct ZE-2 state

(SON), and December–February (DJF). Polar surface air temperature is calculated as an area-weighted mean over 60–90° N for the Arctic and 60–90° S for the Antarctic.

Sea ice area is calculated by integrating grid-cell area multiplied by sea ice concentration over each hemisphere. The sea ice edge is defined using a 15 % sea ice concentration threshold (Notz and SIMIP Community, 2020). Unless otherwise stated, March values in the Arctic and September values in the Antarctic are used to characterise the winter sea ice state.

In the Arctic Ocean, the first ice-free year is defined as the first September with sea ice area below $1 \times 10^6 \mathrm{km}^2$ (Notz and SIMIP Community, 2020). Where the same numerical threshold is applied to Antarctic summer conditions, it is used as an indicator of near-complete sea ice loss rather than as a conventional Antarctic ice-free definition.

2.3 Analysis methods

To standardise multi-model comparisons and remain within the warming range targeted by the Tier-1 protocol, analyses are restricted to the approximate GWL range of -0.5 to $4.5\,^{\circ}\mathrm{C}$ unless otherwise stated.

2.3.1 Polar amplification

We quantify PA using three complementary metrics: 1) transient regression slopes, 2) time-varying amplification ratios, and 3) ratios of mean temperature changes in the zero-emission and post-overshoot states. During UPs, seasonal transient PA is characterised for each model by the slope of a linear regression between seasonal polar SAT anomalies and the corresponding GMSAT anomalies over the first 200 years of the UPs experiment. The fitted slope, expressed in °C/°C, represents the polar

https://doi.org/10.5194/egusphere-2026-6588
Preprint. Discussion started: 22 November 2026
© Author(s) 2026. CC BY 4.0 License.

temperature change per degree of global warming. To examine how PA evolves during warming, we additionally calculate time-varying winter PA as a function of GWL (31-year running-mean annual GMSAT anomaly), using 31-year running-mean polar-to-global SAT anomaly ratios. DJF is used for Arctic winter amplification, and JJA for Antarctic winter amplification. For the zero-emission and post-overshoot experiments, PA is expressed as the ratio between the mean polar SAT anomaly and the corresponding mean GMSAT anomaly, calculated over the first 300 years of each experiment. These diagnostics provide the thermal context for the winter sea ice area and sea ice mass responses.

2.3.2 Warming-level alignment and sea ice hysteresis

To compare sea ice states reached through different climate pathways, simulations are aligned by GWL, defined from the annual GMSAT anomaly relative to the model-specific PI climatology. GWL trajectories are smoothed with a centred 31-year running mean before pathway matching.

We assess sea ice reversibility in two complementary ways. Endpoint reversibility evaluates whether sea ice returns to its PI state when GWL returns to 0°C during ramp-down. The PI-return point is defined by the first downward crossing of 0°C GWL in the 31-year running-mean ramp-down trajectory, and the corresponding sea ice anomaly is linearly interpolated from the 31-year running-mean sea ice trajectory.

Path reversibility is evaluated by comparing ramp-down and ramp-up states at matched GWLs over their common GWL range of 31 years. Sea ice area and mass are smoothed using the same 31-year running mean before matching. Sea ice hysteresis is defined as the ramp-down value minus the corresponding ramp-up value. Negative values indicate delayed or incomplete recovery, whereas positive values indicate over-recovery relative to the ramp-up branch at the same GWL. Matched values are subsequently grouped into 0.5°C GWL bins for model and multi-model summaries.

2.3.3 Thermodynamic sea ice mass-budget diagnostics

Following the framework of Keen et al. (2021), we analyse across ESMs four thermodynamic sea ice mass-budget terms, i.e., basal growth, frazil ice formation, basal melt, and surface melt. Only four ESMs provided these data consistently for all experiments: EC-Earth3-ESM-1, GISS-E2-1-G-CC2, NorESM2-LM, and UKESM1-2-LL. The terms are spatially integrated separately over the Arctic and Antarctic and are evaluated primarily as annual means because the dominant growth and melt processes occur in different seasons.

Three complementary diagnostics are used. First, ramp-up changes are evaluated over the 0–2°C and 2–4°C warming ranges. Second, thermodynamic hysteresis is calculated at matched GWLs as ramp-down minus ramp-up. Growth and melt are converted to positive magnitudes before differencing, so positive values indicate stronger growth or melt during cooling. Third, ZE-2, ZE-4, and Dn4-ZE-2 thermodynamic states are expressed as anomalies relative to the model-specific PI climatology. For the PI-relative diagnostics, native signs are retained: growth is positive and melt negative, so positive melt anomalies indicate reduced ice loss and negative anomalies enhanced ice loss relative to PI.

https://doi.org/10.5194/egusphere-2026-6588
Preprint. Discussion started: 22 November 2026
© Author(s) 2026. CC BY 4.0 License.

These four terms do not constitute a closed sea ice mass budget. Dynamic redistribution and export, lateral melt, snow-ice formation, and other terms are either unavailable or not represented consistently across the four models and are therefore not included.

2.3.4 Multi-model statistics and robustness

Multi-model means and one standard deviation are calculated across all models available for a given experiment and diagnostic. Individual-model results are retained throughout to characterise structural spread across the ensemble. For spatial sea ice concentration differences, sign agreement is evaluated independently at each grid cell. Regions are considered to show ensemble sign agreement where at least six models agree on the sign of the change.

3 Results

3.1 Winter polar amplification and temperature response

Figure 1 summarises the contrasting Arctic and Antarctic temperature responses across the Tier-1 pathways. In the Arctic (60–90° N; Figs. 1a, S1b), the multi-model mean SAT anomaly reaches $4.8 \pm 0.8\,^{\circ}\mathrm{C}$ in ZE-2 and $8.9 \pm 1.8\,^{\circ}\mathrm{C}$ in ZE-4, indicating strong Arctic PA. In the Antarctic (60–90° S; Figs. 1b, S1c), warming generally remains below the corresponding GWL at the ZE-2 (8/10 models) and ZE-4 (6/10 models) branching points but continues under zero emissions in a few models after ZE-2 and more consistently after ZE-4, strengthening Antarctic PA at high GWLs. In Dn4-ZE-2, six models are warmer in the Arctic than in ZE-2, but the multi-model mean is lower, at $4.3 \pm 1.4\,^{\circ}\mathrm{C}$, due to the pronounced negative response of one model (i.e., GISS-E2-1-G-CC2). By contrast, all models are warmer in the Antarctic, where the Dn4-ZE-2 multi-model mean reaches $2.6 \pm 1.2\,^{\circ}\mathrm{C}$ compared with $1.8 \pm 0.9\,^{\circ}\mathrm{C}$ in ZE-2, indicating stronger post-overshoot thermal memory in the Southern Hemisphere.

The ramp-down experiments further reveal contrasting regional recovery. Black markers in Fig. 1 indicate when GWL returns to the PI reference during Dn2 and Dn4; at these points, the polar SAT anomaly does not necessarily return to zero. Figure 1c quantifies these residual anomalies, showing substantial model dependence. GISS-E2-1-G-CC2 exhibits the largest negative Arctic anomaly during Dn4, about 3°C colder than the same anomaly calculated from the PI run at the start of the UP simulation. Positive residuals of around $+1^{\circ}\mathrm{C}$ occur in EC-Earth3-ESM-1 in the Arctic during both Dn2 and Dn4, in GISS-E2-1-G-CC2 and UKESM1-2-LL for Arctic Dn2, and in GISS-E2-1-G-CC2, ACCESS-ESM1-5, GFDL-ESM2M and MIROC-ES2L for Antarctic Dn4. These positive residuals indicate delayed polar thermal recovery relative to the global mean. Thus, GMSAT is reversible by design during Dn2 and Dn4, whereas Arctic and Antarctic temperature responses are not necessarily reversible and can remain strongly pathway-dependent.

During UPs, transient PA is generally strongest in winter and weakest in summer at both poles, although the seasonal dependence is more pronounced in the Arctic than in the Antarctic (Fig. S2). Based on the transient PA slopes, all models show their steepest Arctic SAT–GMSAT relationship in DJF, with slopes of 2.6–3.5°C/°C, consistent with strong wintertime

https://doi.org/10.5194/egusphere-2026-6588
Preprint. Discussion started: 22 November 2026
© Author(s) 2026. CC BY 4.0 License.

Arctic warming reported previously (Pithan and Mauritsen, 2014; Xie et al., 2022; Zhang et al., 2023). Figure 2a summarises the maximum seasonal transient slopes at both poles. Antarctic maxima range from 0.7 to 2.1°C/°C, occurring in JJA for eight models and in MAM for EC-Earth3-ESM-1 and NorESM2-LM. Four models have maximum Antarctic slopes below 1.0, indicating no Antarctic PA according to this metric. The time-varying winter PA ratios show how amplification evolves with GWL during UPs (Fig. 2b). Arctic winter PA generally peaks and then weakens, except in GFDL-ESM2M, whose maximum occurs near the end of the simulation, whereas Antarctic PA tends to increase with GWL. Together, the transient slopes and time-varying ratios support our focus on winter as the thermal context for the sea ice diagnostics below.

Across models, stronger transient Arctic winter PA is associated with an earlier Arctic ice-free year: all six models with transient PA slopes above 3.0°C/°C reach ice-free conditions below 2°C GWL (Figs. 2b,c). However, the first Arctic ice-free year does not generally coincide with peak time-varying PA: seven models peak later, while IPSL-CM6-ESMCO2, CESM2, and GISS-E2-1-G-CC2 peak beforehand (Figs. 2b,d). This link may reflect coupled seasonal processes, with reduced winter ice preconditioning spring–summer melt and summer ice loss enhancing ocean heat uptake, delayed freeze-up, and subsequent cold-season warming (Pithan and Mauritsen, 2014; Chung et al., 2021, 2025). Yet at the first Arctic ice-free year, time-varying Arctic winter PA spans about 2.6–3.7°C/°C, while the corresponding GWL spans about 1.0–3.1 °C, indicating no common threshold across models. Within the analysed ramp-up range of up to 4.5°C GWL, no model reaches near-complete loss of winter Arctic sea ice (Fig. S4). For Antarctic summer, applying the same ice-free threshold of $1 \times 10^6 \mathrm{km}^2$ is less meaningful because several models already have very low initial sea ice states (Fig. S3).

During the zero-emission experiments, Arctic winter PA remains around 2.7–3.9 (Fig. 3a) and is slightly lower in ZE-4 than ZE-2 in all models except CNRM-ESM2-1, while Dn4-ZE-2 generally returns toward ZE-2 except for GISS-E2-1-G-CC2. In contrast, Antarctic PA spans a wider range (0.6–2.5), increases from ZE-2 to ZE-4 in all models except CNRM-ESM2-1, and remains at or above ZE-4 in seven models after overshoot. Accordingly, the multi-model mean changes from about 3.2 to 2.9 for Arctic PA and from 1.2 to 1.6 for Antarctic PA between ZE-2 and ZE-4 (Fig. 3b); in Dn4-ZE-2, Arctic PA returns to about 3.1 when excluding GISS-E2-1-G-CC2, whereas Antarctic PA rises to about 1.7, about 40% stronger after overshoot than at 2°C GWL directly off the ramp-up. This suggests the Arctic adjusts closely to global temperature recovery, whereas the Antarctic retains a stronger thermal memory of the preceding warmer state; this is consistent with slow Southern Ocean adjustment, including ocean heat accumulation during warming and the subsequent resurfacing of the heat during cooling (Chamberlain et al., 2024; King et al., 2024; Li et al., 2025; Frenger et al., 2025). These contrasting polar temperature responses provide the climatic context for the sea ice stability and reversibility examined below.

3.2 Sea ice response along warming and zero-emission pathways

The contrasting winter polar thermal responses are reflected in the corresponding winter sea ice states (Fig. 4). Both sea ice area and mass decline strongly during ramp-up, but the magnitude of change and inter-model spread differ substantially between hemispheres and between the two metrics. Because summer sea ice is strongly depleted at both poles in many models at ZE-2 and is nearly absent at ZE-4 (Fig. S3), we focus below primarily on winter sea ice states, for which differences between zero-emission and post-overshoot states remain more clearly resolved.

https://doi.org/10.5194/egusphere-2026-6588
Preprint. Discussion started: 22 November 2026
© Author(s) 2026. CC BY 4.0 License.

In the Arctic, the first ice-free year occurs across a wide range of concurrent winter sea ice area and mass anomalies, indicating no common winter sea ice state nor unique GWL associated with the onset across models (Fig. 4a,b). Model-specific PI mean states may nevertheless precondition the timing of the first ice-free summer (Massonnet et al., 2018). During UPs and in the ZE-2 and ZE-4 states, inter-model spread is larger for sea ice mass than for area, and mass declines more steeply with warming. This indicates that differences in sea ice thickness contribute in addition to area, such that models with similar ice-covered areas can nevertheless have substantially different sea ice mass and, therefore, volume. Following overshoot, Dn4-ZE-2 generally returns toward the direct ZE-2 state, with the multi-model mean showing a slight over-recovery in both sea ice area and mass.

During ramp-up, GISS-E2-1-G-CC2, CESM2 and NorESM2-LM show comparatively weak Arctic sea ice declines (Fig. S4a). Notably, these models also exhibit AMOC weakening, which may reduce northward ocean heat transport and contribute to the weaker Arctic sea ice loss (Laureanti et al., 2026, in prep.). In contrast, EC-Earth3-ESM-1, UKESM1-2-LL, CNRM-ESM2-1, GFDL-ESM2M and IPSL-CM6-ESMCO2 exhibit a two-stage decline, with accelerated loss at higher GWLs. These model differences are reflected regionally: the Barents and western Kara Seas remain partly ice-covered in models with weaker declines but become largely ice-free with two-stage responses (Fig. S5), consistent with geographically heterogeneous winter sea ice retreat reported in previous studies (Bathiany et al., 2016; Close et al., 2015). Thus, winter Arctic sea ice decline is strongly model dependent.

In the Antarctic, winter sea ice area shows a larger inter-model spread than in the Arctic during UPs and in the ZE-2 and ZE-4 states (Fig. 4c,d), consistent with the larger inter-model spread in Antarctic polar temperature response (Figs. 2b,3b). The ZE-2–ZE-4 separation is more pronounced in sea ice area than in sea ice mass. Although several models continue to decline at ZE-4, the strongest reductions generally occur in models with relatively high PI sea ice states ($> 15 \times 10^6$ km^2) and Antarctic PA > 1 (Figs. 2a, 3b, S4b). IPSL-CM6-ESMCO2 shares these characteristics but shows no comparable ZE-4 decline, indicating that they do not uniquely determine the response. Sea ice mass provides an additional distinction among models through differences in ice thickness. Following overshoot, Dn4-ZE-2 generally remains below the direct ZE-2 state in both sea ice area and mass, in contrast to the slight Arctic over-recovery.

The corresponding spatial patterns further clarify these hemispheric differences (Fig. 5). In the Arctic, the largest winter SIC losses occur mainly along the climatological ice edge and become more extensive in ZE-4, with substantial inter-model differences in the magnitude and spatial extent of winter retreat. The ZE-4–PI difference shows a corridor of SIC loss across the Arctic, with comparatively little change over the Siberian shelf seas, where the shallow bathymetry limits the direct influence of warm Atlantic and Pacific inflows and local hydrographic and thermodynamic conditions dominate (Dmitrenko et al., 2010). Retreat of the winter ice edge increases ocean exposure to the atmosphere and, in some models, may permit wintertime deep mixing farther into the Arctic Ocean (Guo et al., 2026, Laureanti et al., 2026, in prep.). Differences between Dn4-ZE-2 and the direct ZE-2 state are generally small, with localised positive and negative residuals along the ice edge.

In the Antarctic, SIC losses are likewise concentrated in the marginal ice zone, but the additional loss from ZE-2 to ZE-4 is substantially larger than that from PI to ZE-2, indicating a nonlinear response to warming (Fig. 5). Dn4-ZE-2 shows substantially lower SIC than the direct ZE-2 state across a broader area of winter sea ice than the ZE-2–PI difference, despite

https://doi.org/10.5194/egusphere-2026-6588
Preprint. Discussion started: 22 November 2026
© Author(s) 2026. CC BY 4.0 License.

the two ZE-2 states being at similar GWLs. This highlights a pronounced spatial imprint of the preceding overshoot, potentially associated with persistent Southern Ocean heat storage and subsequent release of heat accumulated at higher GWLs during cooling (Ridley and Hewitt, 2014; Lacroix et al., 2024; Frenger et al., 2025). This is consistent with the higher Antarctic PA in Dn4-ZE-2 than in ZE-2 (Fig. 3b). Temporal variability is concentrated mainly along the ice edge and generally becomes more spatially confined as summer sea ice cover retreats (Figs. S5–S8).

The seasonal cycle diagnostics support these pathway differences and show that they are expressed differently in sea ice area and mass across models (Fig. S9). Models differ in the magnitude and seasonality of depletion from ZE-2 to ZE-4, including the pronounced separation identified above in the Antarctic sea ice area, and in the extent to which Dn4-ZE-2 returns toward ZE-2. The four models with available thermodynamic diagnostics span contrasting seasonal and hemispheric responses and are therefore used below as process-based examples to examine their thermodynamic fingerprints.

3.3 Sea ice reversibility and hysteresis during cooling

Arctic winter sea ice area is generally reversible in both Dn2 and Dn4 when GWL returns to 0°C, with little inter-model spread in Dn2 but substantially larger spread in Dn4; GISS-E2-1-G-CC2 shows clear over-recovery in Dn4 (Fig. 6). Antarctic winter sea ice area exhibits larger inter-model spread than in the Arctic. Changes remain limited in Dn2, consistent with relatively weak Antarctic PA in several models (Figs. 2b,3b,S4b), whereas larger departures emerge during Dn4. Sea ice mass is generally less reversible than area, with predominantly negative anomalies in both hemispheres when GWL returns to 0°C; Antarctic Dn2 is the main exception. CNRM-ESM2-1 has no ramp-down simulation, and NorESM2-LM Dn4 shows no clear return to GWL=0°C (Fig. S1a, Harteg et al., submitted).

Because GMSAT is more tightly constrained during ramp-up than ramp-down (Jones et al., 2026), we compare the branches at matched GWLs to assess whether sea ice retraces the warming pathway during cooling. Dn2 generally remains close to UPs, whereas larger departures occur during Dn4 (Fig. 7). In the Arctic, GISS-E2-1-G-CC2 shows pronounced over-recovery throughout Dn4 (Wu et al., 2026), while NorESM2-LM and CESM2 also show over-recovery at higher GWLs but fall below the UPs branch again with further cooling. These changes broadly coincide with AMOC recovery identified in a companion multi-model ocean analysis: GISS-E2-1-G-CC2 retains a strongly weakened AMOC throughout Dn4, accompanied by Arctic cooling to about -3°C relative to PI (Fig. 1c), whereas in NorESM2-LM and CESM2 the AMOC is weaker than during UPs from about 4 to 2°C GWL but strengthens again at lower GWLs (Laureanti et al., 2026, in prep). The transition from sea ice over-recovery to under-recovery is consistent with this evolving ocean heat transport, while most other models remain closer to the ramp-up branch.

In the Antarctic (Fig. 7b), Dn2 likewise remains close to the UPs pathway, while Dn4 shows more consistent under-recovery, with the largest departures below the ramp-up occurring in GISS-E2-1-G-CC2, UKESM1-2-LL, ACCESS-ESM1-5, CESM2 and GFDL-ESM2M. Four of these models also exhibit Antarctic PA > 1 during warming. GFDL-ESM2M is an exception, with PA < 1; Antarctic SAT nevertheless remains about 1.4°C warmer than PI when GWL returns to 0°C (Fig. 1c). Overall, cooling from 4°C produces substantially greater inter-model diversity than cooling from 2°C, with both under- and over-recovery at comparable GWLs.

https://doi.org/10.5194/egusphere-2026-6588
Preprint. Discussion started: 22 November 2026
© Author(s) 2026. CC BY 4.0 License.

Sea ice hysteresis is quantified at matched GWLs as the sea ice state on the cooling branch minus that on the warming branch (Fig. 8), with negative and positive values indicating under- and over-recovery, respectively. Arctic sea ice area shows modest delayed recovery along both Dn2 and Dn4 at lower GWLs (Yu et al., 2025), while the multi-model median approaches zero at higher GWLs with a narrow interquartile range, despite opposing responses in GISS-E2-1-G-CC2 (over-recovery) and EC-Earth3-ESM-1 (under-recovery).

Arctic sea ice mass shows a broadly similar ensemble response but larger model-specific departures, indicating that thickness recovery can differ from area recovery. In EC-Earth3-ESM-1, the strongest negative mass hysteresis occurs toward lower GWLs, suggesting increasingly incomplete thickness recovery as cooling progresses. GISS-E2-1-G-CC2 also shows strong pathway dependence, with weak under-recovery in Dn2 but increasing area and mass toward lower GWLs in Dn4, consistent with recent results showing that strong AMOC weakening after emissions mitigation reduces poleward ocean heat transport, producing pronounced Arctic cooling and sea ice expansion (Wu et al., 2026). Arctic hysteresis is therefore weak in the multi-model median but strongly model dependent, with both delayed recovery and over-recovery across the ensemble.

In the Antarctic, Dn2 shows weak hysteresis, whereas Dn4 exhibits a coherent negative response in both sea ice area and mass (Fig. 8b,d). The strongest negative hysteresis at higher GWLs occurs in GISS-E2-1-G-CC2, UKESM1-2-LL, ACCESS-ESM1-5 and CESM2, broadly coinciding with stronger Antarctic PA (Fig. 2b). At lower GWLs, negative hysteresis persists in some models where Antarctic temperatures remain elevated during cooling, such as in GFDL-ESM2M (Fig. 1c).

Together, the endpoint and matched-GWL diagnostics show that recovery of GWL does not necessarily imply complete or path-independent sea ice recovery. Arctic sea ice generally approaches its PI state with no clear hysteresis but strongly model-dependent recovery trajectories, whereas Antarctic sea ice shows more coherent delayed recovery following the 4°C excursion (Li et al., 2025).

3.4 Thermodynamic fingerprints of contrasting sea ice responses

The four models with thermodynamic diagnostics span the contrasting sea ice responses identified above. EC-Earth3-ESM-1 and NorESM2-LM exhibit strongly Arctic-dominated amplification, UKESM1-2-LL shows a stronger bipolar response, and GISS-E2-1-G-CC2 combines a more moderate hemispheric contrast with pronounced post-overshoot asymmetry (Figs. 2–3). We use these cases to identify the growth and melt signatures associated with their contrasting sea ice evolution.

During ramp-up, Arctic thermodynamic activity generally weakens from 0–2°C to 2–4°C as the ice-covered area contracts (Fig. 9). EC-Earth3-ESM-1 shows the strongest reduction in growth and melt, with NorESM2-LM and UKESM1-2-LL intermediate. Such non-monotonic behaviour is physically plausible because thinner ice and increased open water can initially favour winter growth, while further warming delays freeze-up and shortens the growth season (Cornish et al., 2022; Siew et al., 2025). GISS-E2-1-G-CC2 differs, with basal growth and surface melt increasing at higher GWLs, consistent with its distinct ocean circulation and Arctic cooling response (Sect. 3.3). In the Antarctic, basal melt remains a substantial component of the thermodynamic budget in all four models, highlighting a persistent oceanic contribution to sea ice loss. Surface melt, by contrast, remains weak in EC-Earth3-ESM-1 and NorESM2-LM, consistent with their weaker Antarctic PA, but is more pronounced in GISS-E2-1-G-CC2 and UKESM1-2-LL. This partitioning is consistent with the important role of Southern

https://doi.org/10.5194/egusphere-2026-6588
Preprint. Discussion started: 22 November 2026
© Author(s) 2026. CC BY 4.0 License.

Ocean heat uptake and ocean-to-ice heat flux in regulating Antarctic sea ice (Ridley and Hewitt, 2014). Additional warming therefore modifies the balance between oceanic and atmospheric thermodynamic influences rather than simply scaling the lower-warming response.

Matched-GWL thermodynamic hysteresis further distinguishes the recovery pathways (Fig. 10). In the Arctic, Dn2 is generally associated with weaker growth and melt than during ramp-up, whereas Dn4 shows larger model dependence. GISS-E2-1-G-CC2 and NorESM2-LM develop enhanced basal growth together with enhanced melt during cooling, consistent with the AMOC-associated Arctic cooling described in Sect. 3.3. In GISS-E2-1-G-CC2, these anomalies peak near 2°C GWL and weaken toward lower GWLs. Over the same interval, Arctic SAT falls below PI while sea ice area hysteresis changes little and mass hysteresis continues to increase (Figs. S1b and 8a,c), indicating a transition from areal recovery to continued thickening. The subsequent weakening of basal growth is consistent with the thickness dependence of conductive ice growth, whereby thicker ice grows slower (Bitz and Roe, 2004). NorESM2-LM shows a weaker version of this behaviour, whereas UKESM1-2-LL and EC-Earth3-ESM-1 show modest positive and predominantly negative anomalies, respectively, consistent with their weaker and delayed sea ice recovery during Dn4. In the Antarctic, Dn2 thermodynamic hysteresis is modestly positive, consistent with a sea ice state that remains close to the ramp-up pathway and returns toward PI (Fig. 7b). Dn4 instead shows predominantly negative anomalies above about 1°C GWL, particularly in basal growth and basal melt in GISS-E2-1-G-CC2 and UKESM1-2-LL. Because both growth and melt weaken, the delayed recovery is more consistent with suppressed ice production than with enhanced ice loss. Surface-melt hysteresis is negligible in EC-Earth3-ESM-1 and NorESM2-LM but stronger in GISS-E2-1-G-CC2 and UKESM1-2-LL.

The stabilised and post-overshoot states show related contrasts (Fig. 11). In the Arctic, EC-Earth3-ESM-1, NorESM2-LM and UKESM1-2-LL all show a strong contraction of growth and melt at ZE-4 and a return toward their ZE-2 thermodynamic states in Dn4-ZE-2. The anomaly magnitude broadly covaries with their Arctic PA (Fig. 3). GISS-E2-1-G-CC2 again differs by retaining a more active thermodynamic budget, consistent with its AMOC-associated Arctic cooling and decline of PA toward and below 1.0 in the post-overshoot state.

Antarctic thermodynamic responses are more model dependent. As sea ice becomes depleted (Fig. S4), EC-Earth3-ESM-1 shifts toward frazil formation, whereas basal growth remains more prominent in the other models. Surface-melt anomalies are larger in GISS-E2-1-G-CC2 and UKESM1-2-LL, which also exhibit stronger Antarctic PA. After the 4°C overshoot, EC-Earth3-ESM-1 and UKESM1-2-LL return close to their ZE-2 thermodynamic states, while GISS-E2-1-G-CC2 and NorESM2-LM remain between ZE-2 and ZE-4, indicating a persistent overshoot legacy.

Overall, contrasting sea ice responses emerge from different hemispheric combinations of growth and melt rather than a single thermodynamic control. The same GWL can therefore correspond to different thermodynamic sea ice states, particularly after overshoot, demonstrating that recovery of GMSAT does not imply recovery of the underlying sea ice mass budget.

https://doi.org/10.5194/egusphere-2026-6588
Preprint. Discussion started: 22 November 2026
© Author(s) 2026. CC BY 4.0 License.

4 Discussion

4.1 Stability and reversibility of sea ice across climate pathways

The Tier-1 experiments provide a complementary perspective to conventional transient warming scenarios for distinguishing sea ice responses during warming, zero-emission evolution, cooling and post-overshoot adjustment. This allows us to investigate not only how rapidly sea ice is lost with warming, but whether it approaches a stable state after emissions cease, whether cooling retraces the warming response, and whether the same GWL corresponds to the same polar temperature, sea ice and thermodynamic state after different climate pathways.

The warming and zero-emission experiments show that GWL is not a unique predictor of the polar sea ice state (Sect. 3.2). This pathway dependence is consistent with the different thermal adjustment timescales of the two polar oceans. Strong Arctic PA accompanies rapid sea ice loss during warming, but generally weakens at higher GWLs, whereas Antarctic PA tends to strengthen and remains elevated following overshoot. The latter is consistent with the delayed surface response of the Southern Ocean arising from overturning, heat uptake and redistribution (Armour et al., 2016; Williams et al., 2023). Consequently, returning global temperature toward a previously attained GWL does not necessarily restore the same regional temperature or sea ice state, particularly in the Antarctic. Similar persistence of sea ice anomalies following overshoot has been reported in other multi-model experiments (Roldán-Gómez et al., 2025).

The ramp-down experiments extend this result from thermal memory to reversibility (Sect. 3.3). Arctic sea ice is comparatively reversible at the multi-model level, but individual models span from slightly delayed recovery to pronounced over-recovery, indicating sensitivity to the accompanying ocean-circulation response. GISS-E2-1-G-CC2 provides the clearest example, where strong AMOC weakening and reduced poleward ocean heat transport are associated with Arctic cooling and sea ice expansion (Wu et al., 2026, Laureanti et al., 2026, in prep.). Antarctic recovery is more persistently delayed after the 4°C excursion, particularly in sea ice mass, consistent with the longer adjustment timescale of the Southern Ocean. The ensemble therefore supports pathway-dependent and model-specific recovery, without evidence of a common GWL threshold for abrupt sea ice loss or a single form of hysteresis.

The thermodynamic diagnostics further show that this pathway dependence cannot be reduced to a single sea ice sensitivity or thermodynamic mechanism (Sect. 3.4). Similar sea ice states can be maintained through different combinations of basal growth, frazil formation and melt, while the magnitude of the integrated fluxes also depends on the amount and thickness of ice available to grow or melt (Keen et al., 2021; Bitz and Roe, 2004). The broad contraction of thermodynamic activity with strong warming is consistent across several models, but the balance among individual processes and their recovery differs substantially. Polar temperature therefore provides only part of the explanation: recovery reflects the coupled adjustment of atmosphere, ocean and sea ice, and cannot be inferred from sea ice extent or GWL alone.

The spatial response further illustrates why the coupled background state matters. Winter sea ice retreat occurs mainly along the ice edge (Figs. 5,S5–S8), where increasing ocean exposure can alter surface heat loss and ocean–atmosphere exchange. In EC-Earth3-ESM-1, for example, retreat of winter Arctic sea ice is accompanied by the emergence of new Arctic deep-mixing regions along the retreating ice edge, contributing to a reorganisation of northern deep-water formation (Guo et al.,

https://doi.org/10.5194/egusphere-2026-6588
Preprint. Discussion started: 22 November 2026
© Author(s) 2026. CC BY 4.0 License.

2026). Similar behaviour has been reported in other modelling and observational studies, although the emergence of Arctic deep convection remains uncommon across CMIP6 models (Bretones et al., 2022; Årthun et al., 2025; Heuzé and Liu, 2024). Differences in winter sea ice retreat may therefore contribute to broader inter-model differences in Arctic ocean–atmosphere coupling and PA, although this mechanism is not diagnosed directly here.

The initial PI sea ice state should likewise be viewed as part of this coupled background state rather than as an independent control on the response. Arctic PA is essentially unrelated to PI sea ice area in either winter or summer (both Pearson's correlation coefficients are $r = -0.1$ and $p > 0.5$; not shown), whereas Antarctic PA shows a stronger relationship with winter than summer PI sea ice area (Fig. 12a). Previous work has linked climatological Antarctic sea ice to the spread in Antarctic warming responses (Zhang et al., 2023), but this relationship is embedded within larger differences in Southern Ocean circulation, stratification and heat uptake. In particular, background ocean stratification strongly influences ocean heat-uptake efficiency (Liu et al., 2023) and Antarctic sea ice reversibility under CO_2 removal, with stronger initial stratification favouring upper-ocean heat retention and delayed recovery (Li et al., 2025).

Antarctic PA is more strongly associated with the prescribed ramp-up CO_2-emission rate than with PI sea ice area (Fig. 12b), with models requiring more than 12 Pg C yr^{-1} (see Table 4 in Jones et al., 2026) tending to exhibit PA below 1.0. This relationship is consistent with inter-model differences in Southern Ocean heat uptake and transient climate response (TCR). Models that retain more excess heat near the Southern Ocean surface tend to have stronger surface warming and associated cloud and sea ice feedbacks, yielding higher TCR and larger Antarctic PA; consequently, a lower CO_2-emission rate is required to achieve the prescribed warming rate of 2°C per century. Conversely, models that sequester more heat into the deep ocean tend to have lower TCR and weaker Antarctic PA, requiring larger emissions to reach the same warming rate. Southern Ocean overturning, heat redistribution and associated physical feedbacks therefore contribute substantially to the spread in both Antarctic surface warming and the carbon emissions required to meet this common warming target (Armour et al., 2016; Williams et al., 2023; Gjermundsen et al., 2021).

Taken together, these results show that polar sea ice stability is a property of the coupled climate pathway rather than of GWL alone. The same GWL can correspond to different polar temperatures, sea ice states and thermodynamic balances depending on whether it is reached during warming, cooling or after an overshoot. This distinction is particularly relevant for overshoot pathways, where reversibility cannot be diagnosed directly from transient scenario experiments.

4.2 Structural uncertainty, robustness and limitations

Several qualitative features are robust across the ensemble, while their magnitude, pathway dependence and thermodynamic expression remain strongly model dependent. Sea ice area and mass decline substantially with warming, Arctic winter PA is consistently stronger than Antarctic winter PA, and cooling does not generally retrace the warming pathway. Antarctic sea ice shows more robust delayed recovery during cooling from 4°C GWL, particularly in sea ice mass, whereas Arctic hysteresis is weaker in the multi-model response, with model-to-model differences in delayed recovery and over-recovery closely linked to the corresponding AMOC recovery, non-recovery or over-recovery. The same GWL can therefore correspond to different polar

https://doi.org/10.5194/egusphere-2026-6588
Preprint. Discussion started: 22 November 2026
© Author(s) 2026. CC BY 4.0 License.

temperature, sea ice and thermodynamic states depending on pathway history. These conclusions are supported consistently across trajectory, matched-GWL, spatial, seasonal and thermodynamic diagnostics.

However, ensemble size and diagnostic availability limit the robustness of these conclusions. The analysis includes ten models for sea ice and temperature, nine with ramp-down experiments, and only four with the major thermodynamic mass-budget terms required for process attribution. The four-model thermodynamic analysis should therefore be interpreted as a set of contrasting process examples rather than a statistically representative sample. Likewise, the response types identified here are descriptive archetypes with overlapping behaviour, not discrete or formally defined model clusters.

The available thermodynamic diagnostics represent only part of the sea ice mass balance. We restrict the analysis to basal growth, frazil formation, basal melt and surface melt because dynamic redistribution and export, lateral melt, snow-ice formation and other terms are unavailable or not represented consistently across models. Dynamic processes may nevertheless be important, particularly during extreme Arctic sea ice reductions, for which sea ice motion can contribute comparably to thermodynamic effects (Li et al., 2026). The diagnosed thermodynamic fingerprints therefore capture important components of the response but do not provide a closed attribution of total sea ice mass change. Recovery may additionally be modulated by AMOC-driven changes in ocean heat transport and mixed-layer heat storage, as well as by feedbacks involving atmospheric energy fluxes and sea ice dynamics. Recent work highlights the role of ocean-circulation changes in Arctic cooling and sea ice expansion during mitigation pathways (Wu et al., 2026, Laureanti et al., 2026, in prep.).

Further uncertainty in the interpretation of Antarctic behaviour arises from substantial inter-model differences in the pre-industrial climatological sea ice state (Roach et al., 2020), which have been linked to the spread in Antarctic warming responses (Zhang et al., 2023), as well as from differences in the representation of dynamic and thermodynamic sea ice processes (Nie et al., 2023). Integrated thermodynamic fluxes depend on the amount of ice available to grow or melt (Keen et al., 2021), so mean-state differences can affect the magnitude of diagnosed budget anomalies and complicate direct process comparisons across models. More broadly, the contrasting Arctic and Antarctic responses reinforce the need for a coupled perspective, as sea ice variability in both hemispheres reflects interacting oceanic and atmospheric processes whose representation remains a source of model uncertainty (Spira et al., 2026).

These limitations also highlight the value of placing the sea ice analysis within the broader set of TIPMIP multi-model assessments. Recent overshoot studies likewise show that incomplete sea ice recovery can coexist with persistent changes in meridional overturning and ocean heat transport, with the relative contribution of these mechanisms varying substantially among models (Roldán-Gómez et al., 2025). Companion TIPMIP-Ocean analyses, including experiments with induced radiative warming and freshwater discharges (Swingedouw et al., 2026), can further constrain the role of persistent circulation and heat-uptake anomalies in delayed sea ice recovery. In GISS-E2-1-G-CC2, particularly slow AMOC recovery is consistent with reduced poleward ocean heat transport and associated Arctic cooling driven by radiative warming at 1% CO_2 increase and reported by Wu et al. (2026). Complementary surface-climate analyses can clarify the roles of atmospheric warming, radiative feedbacks, meridional heat transport and circulation changes in shaping PA and the regional recovery of sea ice (Mahmood et al., 2026, in prep.). Linking the sea ice response to the evolution of the coupled atmosphere–ocean system, rather than interpreting the ice budget in isolation, should therefore provide a more complete attribution of overshoot memory.

https://doi.org/10.5194/egusphere-2026-6588
Preprint. Discussion started: 22 November 2026
© Author(s) 2026. CC BY 4.0 License.

4.3 Implications for model assessment

The thermodynamic diagnostics provide a process-based basis for model evaluation. Models at similar GWLs can exhibit similar sea ice area while maintaining those states through different combinations of growth and melt, such that evaluation based only on sea ice extent or concentration may conceal compensating process errors. Combining sea ice area, mass and process-level budget diagnostics therefore provides a more stringent test of whether similar sea ice states arise for physically consistent reasons.

The distinction between GWL and pathway history is also important for climate risk assessment. Polar conditions at the same GWL can differ depending on whether that level is reached directly during warming or by cooling from a transient overshoot, particularly in the Antarctic. In the Arctic, pathway dependence can also arise through ocean-circulation changes: in several models, AMOC weakening during cooling coincides with reduced poleward ocean heat transport, pronounced Arctic cooling and sea ice expansion. Overshoot assessments should therefore take into account not only peak and final global warming, but also the persistence of regional thermal, ocean-circulation and cryospheric anomalies during recovery. Such sea ice anomalies may in turn influence atmospheric circulation and climate extremes beyond the polar region, although the strength and causality of these Arctic–midlatitude linkages remain uncertain (IPCC, 2021).

More broadly, the TIPMIP framework shows the benefit of coordinated pathway experiments to distinguish transient response, zero-emission evolution and reversibility (Jones et al., 2026; Winkelmann et al., 2025). Applying the same framework to sea ice, ocean circulation, surface climate and other Earth-system components can help identify which parts of the climate system recover mainly with global temperature and which have more long-lived memory of the pathway taken to reach that state.

5 Conclusions

Polar sea ice has been discussed as a potential tipping element in the Earth system. Here, we investigate its stability and reversibility across the coordinated TIPMIP-ESM Tier-1 warming, zero-emission, cooling and post-overshoot experiments. While no common GWL threshold emerges for the first Arctic ice-free summer across models, GMSAT alone does not control the recovery of polar sea ice. By design, GMSAT is reversible during cooling, whereas Arctic and Antarctic temperatures are not, and cooling therefore does not generally retrace warming at the regional scale. Arctic winter sea ice is relatively reversible in the multi-model response, although individual models show delayed recovery or over-recovery closely linked to the corresponding AMOC recovery, non-recovery or over-recovery. In contrast, Antarctic sea ice more consistently fails to retrace the warming pathway, with persistent delayed recovery following strong overshoot. Thermodynamic diagnostics show that these responses arise from different combinations of ice production and melt and depend on the underlying sea ice state. The coordinated pathway experiments therefore provide information on sea ice stability and reversibility that cannot be obtained from transient warming simulations alone. Future work should extend such pathway-based analyses to larger model ensembles and more complete sea ice mass-budget diagnostics, while linking sea ice recovery more directly to ocean and

https://doi.org/10.5194/egusphere-2026-6588
Preprint. Discussion started: 22 November 2026
© Author(s) 2026. CC BY 4.0 License.

surface-climate responses. A further priority is to identify robust regional or process-based indicators of threshold-like winter sea ice loss and test their robustness across models and climate pathways.

Appendix A

This appendix summarises the Earth system models included in the TIPMIP Tier-1 sea ice multi-model analysis. For each model, Table A1 lists the atmospheric, ocean and sea ice components together with their nominal resolutions and the corresponding model reference. Models with available sea ice mass-budget diagnostics are additionally identified in the table.

Table A1. Earth system models included in the TIPMIP Tier-1 sea ice analysis.

Model	Atmosphere	Ocean	Sea ice	Ice sheet	Reference
a. EC-Earth3-ESM-1*	IFS cy36r4; 80km; L91	NEMO3.6; 100km; L75	LIM3; $\rho_{\mathrm{ice}} = 917\ \mathrm{kg\,m^{-3}}$	GrIS: PISM; AIS: freshwater emulator	Doescher et al. (2022), Guo et al. (2026)
b. GISS-E2-1-G-CC2* (NASA-GISS)	GISS-E2.1; 250km; L40	GISS Ocean; 100km; L40	GISS sea ice model; $\rho_{\mathrm{ice}} = 916.6\ \mathrm{kg\,m^{-3}}$	GrIS/AIS: prescribed	Romanou et al. (2026)
c. NorESM2-LM*	CAM6-Nor; 250km; L32	BLOM; 100km; L70	CICE5.1.2; $\rho_{\mathrm{ice}} = 917\ \mathrm{kg\,m^{-3}}$	GrIS/AIS: prescribed	Seland et al. (2020)
d. UKESM1-2-LL*	MetUM-HadGEM3-GA7.1; 250km; L85	NEMO-HadGEM3-GO6.0; 100km; L75	CICE-HadGEM3-GSI8, $\rho_{\mathrm{ice}} = 917\ \mathrm{kg\,m^{-3}}$	GrIS/AIS: BISICLES coupled	Sellar et al. (2019), Smith et al. (2021), Mulcahy et al. (2023)
e. ACCESS-ESM1-5	UM7.3 (∼GA1); 250km; L38	MOM5; 100km; L50	CICE4.1; $\rho_{\mathrm{ice}} = 917\ \mathrm{kg\,m^{-3}}$	GrIS/AIS: prescribed	Ziehn et al. (2020)
f. CESM2	CAM6; 100km; L32	POP2; 100km; L60	CICE5.1; $\rho_{\mathrm{ice}} = 917\ \mathrm{kg\,m^{-3}}$	GrIS: CISM available; AIS: prescribed	Danabasoglu et al. (2020)
g. CNRM-ESM2-1†	Arpege 6.3;250km; L91	Nemo 3.6; 100km; L75	Gelato 6.1; $\rho_{\mathrm{ice}} = 910\ \mathrm{kg\,m^{-3}}$	GrIS/AIS: prescribed	Séférian et al. (2019)
h. GFDL-ESM2M	AM2; 250km; L24	MOM4p1; 100km; L50	SIM2; $\rho_{\mathrm{ice}} = 905\ \mathrm{kg\,m^{-3}}$	GrIS/AIS: prescribed	Dunne et al. (2013)
i. IPSL-CM6-ESMCO2	LMDZ; 250km; L79	NEMO-OPA; 100km; L75	LIM3; $\rho_{\mathrm{ice}} = 917\ \mathrm{kg\,m^{-3}}$	GrIS/AIS: prescribed	Boucher et al. (2020)
j. MIROC-ES2L	CCSR AGCM; 500km; L40	COCO4.9; 100km; L63	COCO4.9; $\rho_{\mathrm{ice}} = 900\ \mathrm{kg\,m^{-3}}$	GrIS/AIS: prescribed	Hajima et al. (2020)

* Models with available sea ice mass-budget diagnostics.

† The number of sea ice thickness categories could not be confirmed for the marked models; all other models use multiple thickness categories.

GrIS: Greenland Ice Sheet; AIS: Antarctic Ice Sheet.

https://doi.org/10.5194/egusphere-2026-6588
Preprint. Discussion started: 22 November 2026
© Author(s) 2026. CC BY 4.0 License.

Code availability.

The codes used for data preprocessing are publicly available through the *Sea Ice Mass Budget Analysis: Model Intercomparison Project* repository at https://github.com/oj-tooth/SeaIceMassBudgetMIP.

This repository supports the TIPMIP Tier-1 multi-model sea ice mass-balance analysis developed by Tian Tian and Oliver Tooth. The analysis further quantifies the relative contributions of individual sea ice mass-budget terms following the framework of Keen et al. (2021).

Data availability.

The TIPMIP ESM Tier-1 model output analysed in this study is available from the corresponding project repositories and contributing institutions. Some datasets are already available through ESGF, and the remaining model output will be published there progressively. The processed diagnostics and analysis-ready datasets generated in this study will be made available upon publication.

Author contributions.

TiT and SY conceived the study. TiT designed the analysis. TiT and OT developed the preprocessing tools, and TiT, OT and ThT processed the model output. All authors contributed to the model simulations and data production. TiT performed the analysis, with interpretation and discussion of the results involving all authors. TiT wrote the initial draft of the manuscript, and all authors contributed to its revision.

Competing interests. The authors declare no conflict of interest.

Acknowledgements. We acknowledge the Tipping Points Modelling Intercomparison Project (TIPMIP) and its participants for producing and publishing their simulation data. We thank the Max-Planck Institute of Geoanthropology (MPI-GEA) and the Potsdam Institute for Climate Impact Research (PIK) for coordinating TIPMIP and providing the infrastructure necessary to advance the project. We also thank the many people and institutions behind the Coupled Model Intercomparison Project (CMIP) and the Earth System Grid Federation (ESGF) for their guidance and support of initiatives such as TIPMIP. This is TIPMIP contribution #006. This work used resources of the Deutsches Klimarechenzentrum (DKRZ) granted by its Scientific Steering Committee (WLA) under project ID bm1448. **Funding:** This research has been supported by the Danish National Center for Climate Research (NCKF), funded by the Danish government, and the Horizon Europe projects TipESM "Exploring Tipping Points and Their Impacts Using Earth System Models" (grant agreement no. 101137673; DOI: 10.3030/101137673, TipESM contribution no. 57), and OptimESM "Optimal High Resolution Earth System Models for Exploring Future Climate Change" (grant agreement no. 101081193).

https://doi.org/10.5194/egusphere-2026-6588
Preprint. Discussion started: 22 November 2026
© Author(s) 2026. CC BY 4.0 License.

References

Angevaare, J. R. and Drijfhout, S. S.: Catalogue of strong nonlinear surprises in ocean, sea-ice, and atmospheric variables in CMIP6, Earth System Dynamics, 17, 1081–1115, https://doi.org/10.5194/esd-17-1081-2026, 2026.

Armour, K. C., Eisenman, I., Blanchard-Wrigglesworth, E., McCusker, K. E., and Bitz, C. M.: The reversibility of sea ice loss in a state-of-the-art climate model, Geophysical Research Letters, 38, L16 705, https://doi.org/10.1029/2011GL048739, 2011.

Armour, K. C., Marshall, J., Scott, J. R., Donohoe, A., and Newsom, E. R.: Southern Ocean warming delayed by circumpolar upwelling and equatorward transport, Nature Geoscience, 9, 549–554, https://doi.org/10.1038/ngeo2731, 2016.

Årthun, M., Brakstad, A., Dörr, J., Johnson, H. L., Mans, C., Semper, S., and Våge, K.: Atlantification drives recent strengthening of the Arctic overturning circulation, Science Advances, 11, eadu1794, https://doi.org/10.1126/sciadv.adu1794, 2025.

Bathiany, S., Notz, D., Mauritsen, T., Raedel, G., and Brovkin, V.: On the potential for abrupt Arctic winter sea ice loss, Journal of Climate, 29, 2703–2719, https://doi.org/10.1175/JCLI-D-15-0466.1, 2016.

Bitz, C. M. and Roe, G. H.: A mechanism for the high rate of sea ice thinning in the Arctic Ocean, Journal of Climate, 17, 3623 – 3632, https://doi.org/10.1175/1520-0442(2004)017<3623:AMFTHR>2.0.CO;2, 2004.

Boucher, O., Servonnat, J., Albright, A. L., Aumont, O., Balkanski, Y., Bastrikov, V., Bekki, S., Bonnet, R., Bony, S., Bopp, L., Braconnot, P., Brockmann, P., Cadule, P., Caubel, A., Cheruy, F., Codron, F., Cozic, A., Cugnet, D., D'Andrea, F., Davini, P., de Lavergne, C., Denvil, S., Deshayes, J., Devilliers, M., Ducharne, A., Dufresne, J.-L., Dupont, E., Ethé, C., Fairhead, L., Falletti, L., Flavoni, S., Foujols, M.-A., Gardoll, S., Gastineau, G., Ghattas, J., Grandpeix, J.-Y., Guenet, B., Guez, L., Guilyardi, E., Guimberteau, M., Hauglustaine, D., Hourdin, F., Idelkadi, A., Joussaume, S., Kageyama, M., Khadre-Traoré, A., Khodri, M., Krinner, G., Lebas, N., Levavasseur, G., Lévy, C., Li, L., Lott, F., Lurton, T., Luyssaert, S., Madec, G., Madeleine, J.-B., Maignan, F., Marchand, M., Marti, O., Mellul, L., Meurdesoif, Y., Mignot, J., Musat, I., Ottlé, C., Peylin, P., Planton, Y., Polcher, J., Rio, C., Rochetin, N., Rousset, C., Sepulchre, P., Sima, A., Swingedouw, D., Thieblemont, R., Traoré, A., Vancoppenolle, M., Vial, J., Vialard, J., Viovy, N., and Vuichard, N.: Presentation and evaluation of the IPSL-CM6A-LR climate model, Journal of Advances in Modeling Earth Systems, 12, e2019MS002 010, https://doi.org/10.1029/2019MS002010, 2020.

Bretones, A., Nisancioglu, K. H., Jensen, M. F., Brakstad, A., and Yang, S.: Transient increase in Arctic deep-water formation and ocean circulation under sea ice retreat, Journal of Climate, 35, 109–124, https://doi.org/10.1175/JCLI-D-21-0152.1, 2022.

Chamberlain, M. A., Ziehn, T., and Law, R. M.: The Southern Ocean as the climate's freight train – driving ongoing global warming under zero-emission scenarios with ACCESS-ESM1.5, Biogeosciences, 21, 3053–3073, https://doi.org/10.5194/bg-21-3053-2024, 2024.

Chung, E.-S., Ha, K.-J., Timmermann, A., Stuecker, M. F., Bodai, T., and Lee, S.-K.: Cold-season Arctic amplification driven by Arctic Ocean-mediated seasonal energy transfer, Earth's Future, 9, e2020EF001 898, https://doi.org/10.1029/2020EF001898, 2021.

Chung, E.-S., Kim, S.-J., Ha, K.-J., et al.: The role of sea ice in present and future Arctic amplification, Communications Earth & Environment, 6, 910, https://doi.org/10.1038/s43247-025-02834-9, 2025.

Close, S., Houssais, M.-N., and Herbaut, C.: Regional dependence in the timing of onset of rapid decline in Arctic sea ice concentration, Journal of Geophysical Research: Oceans, 120, 8077–8098, https://doi.org/10.1002/2015JC011187, 2015.

Cornish, S., Johnson, H., Mallett, R., Dörr, J., Kostov, Y., and Richards, A.: Rise and fall of sea ice production in the Arctic Ocean's ice factories, Nature Communications, 13, 7800, https://doi.org/10.1038/s41467-022-34785-6, 2022.

Danabasoglu, G., Lamarque, J.-F., Bacmeister, J., Bailey, D. A., DuVivier, A. K., Edwards, J., Emmons, L. K., Fasullo, J., Garcia, R., Gettelman, A., Hannay, C., Holland, M. M., Large, W. G., Lauritzen, P. H., Lawrence, D. M., Lenaerts, J. T. M., Lindsay, K., Lipscomb,

https://doi.org/10.5194/egusphere-2026-6588
Preprint. Discussion started: 22 November 2026
© Author(s) 2026. CC BY 4.0 License.



W. H., Mills, M. J., Neale, R., Oleson, K. W., Otto-Bliesner, B., Phillips, A. S., Sacks, W., Tilmes, S., van Kampenhout, L., Vertenstein, M., Bertini, A., Dennis, J., Deser, C., Fischer, C., Fox-Kemper, B., Kay, J. E., Kinnison, D., Kushner, P. J., Larson, V. E., Long, M. C., Mickelson, S., Moore, J. K., Nienhouse, E., Polvani, L., Rasch, P. J., and Strand, W. G.: The Community Earth System Model Version 2 (CESM2), Journal of Advances in Modeling Earth Systems, 12, e2019MS001 916, https://doi.org/10.1029/2019MS001916, 2020.

Dmitrenko, I. A., Kirillov, S. A., Tremblay, L. B., Bauch, D., Hölemann, J. A., Krumpen, T., Kassens, H., Wegner, C., Heinemann, G., and Schröder, D.: Impact of the Arctic Ocean Atlantic water layer on Siberian shelf hydrography, Journal of Geophysical Research: Oceans, 115, C08 010, https://doi.org/10.1029/2009JC006020, 2010.

Doescher, R., Acosta, M., Alessandri, A., and the EC-Earth Consortium: The EC-Earth3 Earth System Model for the Climate Model Intercomparison Project 6, Geosci. Model Dev., 15, 2973–3020, https://doi.org/10.5194/gmd-15-2973-2022, 2022.

Dunne, J. P., John, J. G., Shevliakova, E., Stouffer, R. J., Krasting, J. P., Malyshev, S. L., Milly, P. C. D., Sentman, L. T., Adcroft, A. J., Cooke, W., Dunne, K. A., Griffies, S. M., Hallberg, R. W., Harrison, M. J., Levy, H., Wittenberg, A. T., Phillips, P. J., and Zadeh, N.: GFDL's ESM2 global coupled climate–carbon earth system models. Part II: carbon system formulation and baseline simulation characteristics, Journal of Climate, 26, 2247–2267, https://doi.org/10.1175/JCLI-D-12-00150.1, 2013.

Frenger, I., Frey, S., Oschlies, A., Getzlaff, J., Martin, T., and Koeve, W.: Southern Ocean heat burp in a cooling world, AGU Advances, 6, e2025AV001 700, https://doi.org/10.1029/2025AV001700, 2025.

Gjermundsen, A., Nummelin, A., Olivié, D., Bentsen, M., Seland, Ø., and Schulz, M.: Shutdown of Southern Ocean convection controls long-term greenhouse gas-induced warming, Nature Geoscience, 14, 724–731, https://doi.org/10.1038/s41561-021-00825-x, 2021.

Guo, C., Yang, S., Schiller-Weiss, I., Bernales, J., Olsen, S. M., Koenigk, T., Mahmood, R., Tian, T., and Wyser, K.: Reversible Atlantic overturning despite continued Greenland ice sheet melt, Science Advances, 12, eaee5373, https://doi.org/10.1126/sciadv.aee5373, 2026.

Hajima, T., Watanabe, M., Yamamoto, A., Tatebe, H., Noguchi, M. A., Abe, M., Ohgaito, R., Ito, A., Yamazaki, D., Okajima, H., Ito, A., Takata, K., Ogochi, K., Watanabe, S., and Kawamiya, M.: Development of the MIROC-ES2L Earth system model and the evaluation of biogeochemical processes and feedbacks, Geoscientific Model Development, 13, 2197–2244, https://doi.org/10.5194/gmd-13-2197-2020, 2020.

Heuzé, C. and Liu, H.: No emergence of deep convection in the Arctic Ocean across CMIP6 models, Geophysical Research Letters, 51, e2023GL106 499, https://doi.org/10.1029/2023GL106499, 2024.

Holmes, C. R., Bracegirdle, T. J., and Holland, P. R.: Antarctic sea ice projections constrained by historical ice cover and future global temperature change, Geophysical Research Letters, 49, e2021GL097 413, https://doi.org/10.1029/2021GL097413, 2022.

IPCC: Climate Change 2021: The Physical Science Basis, Cambridge University Press, contribution of Working Group I to the Sixth Assessment Report of the Intergovernmental Panel on Climate Change, https://doi.org/10.1017/9781009157896, 2021.

Jones, C., Bossert, I., Dennis, D. P., Jeffery, H. A., Jones, C. D., Koenigk, T., Loriani, S., Sanderson, B., Séférian, R., Wyser, K., Yang, S., Abe, M., Bathiany, S., Braconnot, P., Brovkin, V., Burger, F. A., Cadule, P., Castruccio, F. S., Danabasoglu, G., Dittus, A., Donges, J. F., Fröb, F., Frölicher, T. L., Georgievski, G., Guo, C., Hu, A., Lawrence, P., Lerner, P., Licón-Saláiz, J., Otto-Bliesner, B., Romanou, A., Shevliakova, E., Silvy, Y., Swingedouw, D., Tjiputra, J., Walton, J., Wiltshire, A., Winkelmann, R., Wood, R., Yokohata, T., and Ziehn, T.: The TIPMIP Earth system model experiment protocol: phase 1, Geoscientific Model Development, 19, 6941–6966, https://doi.org/10.5194/gmd-19-6941-2026, 2026.

Keen, A., Blockley, E., Bailey, D. A., Boldingh Debernard, J., Bushuk, M., Delhaye, S., Docquier, D., Feltham, D., Massonnet, F., O'Farrell, S., Ponsoni, L., Rodriguez, J. M., Schroeder, D., Swart, N., Toyoda, T., Tsujino, H., Vancoppenolle, M., and Wyser, K.: An inter-

https://doi.org/10.5194/egusphere-2026-6588
Preprint. Discussion started: 22 November 2026
© Author(s) 2026. CC BY 4.0 License.

comparison of the mass budget of the Arctic sea ice in CMIP6 models, The Cryosphere, 15, 951–982, https://doi.org/10.5194/tc-15-951-2021, 2021.

King, A. D., Ziehn, T., Chamberlain, M., Borowiak, A. R., Brown, J. R., Cassidy, L., Dittus, A. J., Grose, M., Maher, N., Paik, S., Perkins-Kirkpatrick, S. E., and Sengupta, A.: Exploring climate stabilisation at different global warming levels in ACCESS-ESM-1.5, Earth System Dynamics, 15, 1353–1383, https://doi.org/10.5194/esd-15-1353-2024, 2024.

Lacroix, F., Burger, F. A., Silvy, Y., Schleussner, C.-F., and Frölicher, T. L.: Persistently elevated high-latitude ocean temperatures and global sea level following temporary temperature overshoots, Earth's Future, 12, e2024EF004 862, https://doi.org/10.1029/2024EF004862, 2024.

Li, S., Hu, K., Huang, G., and Zheng, X.-T.: The reversibility of Antarctic sea ice loss under CO_2 removal scenarios, Geophysical Research Letters, 52, e2025GL116 756, https://doi.org/10.1029/2025GL116756, 2025.

Li, Z., Ding, R., Huang, F., et al.: Two modes of extreme central Arctic sea ice reduction: temperature advection and sea ice motion dominance, Climate Dynamics, 64, 92, https://doi.org/10.1007/s00382-026-08052-z, 2026.

Linke, O., Lenhardt, J., Lund, M. T., Merikanto, J., Naakka, T., Nordling, K., Räisänen, P., Samset, B. H., Thomas, J. L., and Ekman, A. M. L.: Understanding the spread in climate feedbacks and polar amplification using coordinated multi-model experiments and CMIP6, Journal of Climate, 39, 4049 – 4070, https://doi.org/10.1175/JCLI-D-25-0551.1, 2026.

Liu, M., Soden, B. J., Vecchi, G. A., and Wang, C.: The spread of ocean heat uptake efficiency traced to ocean salinity, Geophysical research letters, 50, e2022GL100 171, https://doi.org/10.1029/2022GL100171, 2023.

Massonnet, F., Vancoppenolle, M., Goosse, H., Docquier, D., Fichefet, T., and Blanchard-Wrigglesworth, E.: Arctic sea-ice change tied to its mean state through thermodynamic processes, Nature Climate Change, 8, 599–603, https://doi.org/10.1038/s41558-018-0204-z, 2018.

Mulcahy, J. P., Jones, C. G., Rumbold, S. T., Kuhlbrodt, T., Dittus, A. J., Blockley, E. W., Yool, A., Walton, J., Hardacre, C., Andrews, T., Bodas-Salcedo, A., Stringer, M., de Mora, L., Harris, P., Hill, R., Kelley, D., Robertson, E., and Tang, Y.: UKESM1.1: development and evaluation of an updated configuration of the UK Earth System Model, Geoscientific Model Development, 16, 1569–1600, https://doi.org/10.5194/gmd-16-1569-2023, 2023.

Nie, Y., Lin, X., Yang, Q., Liu, J., Chen, D., and Uotila, P.: Differences between the CMIP5 and CMIP6 Antarctic sea ice concentration budgets, Geophysical Research Letters, 50, e2023GL105 265, https://doi.org/10.1029/2023GL105265, 2023.

Notz, D. and SIMIP Community: Arctic sea ice in CMIP6, Geophysical Research Letters, 47, e2019GL086 749, https://doi.org/10.1029/2019GL086749, 2020.

Pithan, F. and Mauritsen, T.: Arctic amplification dominated by temperature feedbacks in contemporary climate models, Nature Geoscience, 7, 181–184, https://doi.org/10.1038/ngeo2071, 2014.

Ridley, J. K. and Hewitt, H. T.: A mechanism for lack of sea ice reversibility in the Southern Ocean, Geophysical Research Letters, 41, 8404–8410, https://doi.org/10.1002/2014GL062167, 2014.

Roach, L. A., Dörr, J., Holmes, C. R., Massonnet, F., Blockley, E. W., Notz, D., et al.: Antarctic sea ice area in CMIP6, Geophysical Research Letters, 47, e2019GL086 729, https://doi.org/10.1029/2019GL086729, 2020.

Roldán-Gómez, P. J., Ortega, P., and Donat, M. G.: Contribution of meridional overturning circulation and sea ice changes to large-scale temperature asymmetries in CMIP6 overshoot scenarios, Ocean Science, 21, 2283–2303, https://doi.org/10.5194/os-21-2283-2025, 2025.

Romanou, A., Lerner, P., Romanski, J., Kiang, N. Y., Aleinov, I., Kelley, M., Miller, R. L., Russell, G., Ruedy, R., Schmidt, G. A., Hakuba, M. Z., and Wang, O.: The NASA-GISS ModelE2.1-CC2 ESM: development and evaluation, Geoscientific Model Development, 19, 9131–9176, https://doi.org/10.5194/gmd-19-9131-2026, 2026.

https://doi.org/10.5194/egusphere-2026-6588
Preprint. Discussion started: 22 November 2026
© Author(s) 2026. CC BY 4.0 License.

Romanou, A. et al.: Stochastic Bifurcation of the North Atlantic Circulation under a Midrange Future Climate Scenario with the NASA-GISS ModelE, Journal of Climate, 36, 6141–6161, https://doi.org/10.1175/JCLI-D-22-0536.1, 2023.

Schwinger, J., Asaadi, A., Goris, N., and Lee, H.: Possibility for strong northern hemisphere high-latitude cooling under negative emissions, Nature Communications, 13, 1095, https://doi.org/10.1038/s41467-022-28573-5, 2022.

Screen, J. A. and Simmonds, I.: Increasing fall-winter energy loss from the Arctic Ocean and its role in Arctic temperature amplification, Geophysical Research Letters, 37, L16 707, https://doi.org/10.1029/2010GL044136, 2010a.

Screen, J. A. and Simmonds, I.: The central role of diminishing sea ice in recent Arctic temperature amplification, Nature, 464, 1334–1337, https://doi.org/10.1038/nature09051, 2010b.

Séférian, R., Nabat, P., Michou, M., Saint-Martin, D., Voldoire, A., Colin, J., Decharme, B., Delire, C., Berthet, S., Chevallier, M., Sénési, S., Franchisteguy, L., Vial, J., Mallet, M., Joetzjer, E., Geoffroy, O., Guérémy, J.-F., Moine, M.-P., Msadek, R., Ribes, A., Rocher, M., Roehrig, R., Salas-y Mélia, D., Sanchez, E., Terray, L., Valcke, S., Waldman, R., Aumont, O., Bopp, L., Deshayes, J., Éthé, C., and Madec, G.: Evaluation of CNRM Earth System Model, CNRM-ESM2-1: Role of Earth System Processes in Present-Day and Future Climate, Journal of Advances in Modeling Earth Systems, 11, 4182–4227, https://doi.org/10.1029/2019MS001791, 2019.

Seland, Ø., Bentsen, M., Olivié, D., Toniazzo, T., Gjermundsen, A., Graff, L. S., Debernard, J. B., Gupta, A. K., He, Y.-C., Kirkevåg, A., Schwinger, J., Tjiputra, J., Aas, K. S., Bethke, I., Fan, Y., Griesfeller, J., Grini, A., Guo, C., Ilicak, M., Karset, I. H. H., Landgren, O., Liakka, J., Moseid, K. O., Nummelin, A., Spensberger, C., Tang, H., Zhang, Z., Heinze, C., Iversen, T., and Schulz, M.: Overview of the Norwegian Earth System Model (NorESM2) and key climate response of CMIP6 DECK, historical, and scenario simulations, Geoscientific Model Development, 13, 6165–6200, https://doi.org/10.5194/gmd-13-6165-2020, 2020.

Sellar, A. A., Jones, C. G., Mulcahy, J. P., Tang, Y., Yool, A., Wiltshire, A., O'Connor, F. M., Stringer, M., Hill, R., Palmieri, J., Woodward, S., de Mora, L., Kuhlbrodt, T., Rumbold, S. T., Kelley, D. I., Ellis, R., Johnson, C. E., Walton, J., Abraham, N. L., Andrews, M. B., Andrews, T., Archibald, A. T., Berthou, S., Burke, E., Blockley, E., Carslaw, K., Dalvi, M., Edwards, J., Folberth, G. A., Gedney, N., Griffiths, P. T., Harper, A. B., Hendry, M. A., Hewitt, A. J., Johnson, B., Jones, A., Jones, C. D., Keeble, J., Liddicoat, S., Morgenstern, O., Parker, R. J., Predoi, V., Robertson, E., Siahaan, A., Smith, R. S., Swaminathan, R., Woodhouse, M. T., Zeng, G., and Zerroukat, M.: UKESM1: Description and Evaluation of the U.K. Earth System Model, Journal of Advances in Modeling Earth Systems, 11, 4513–4558, https://doi.org/10.1029/2019MS001739, 2019.

Serreze, M. C. and Barry, R. G.: Processes and impacts of Arctic amplification: A research synthesis, Global and planetary change, 77, 85–96, https://doi.org/10.1016/j.gloplacha.2011.03.004, 2011.

Siew, P. Y. F., Wu, Y., Ting, M., and Zheng, C.: Identifying physical drivers of Arctic sea ice growth and their changing roles in a warming climate, Geophysical Research Letters, 52, e2024GL113 601, 2025.

Smith, R. S., Mathiot, P., Siahaan, A., Lee, V., Cornford, S. L., Gregory, J. M., Payne, A. J., Jenkins, A., Holland, P. R., Ridley, J. K., and Jones, C. G.: Coupling the U.K. Earth System Model to Dynamic Models of the Greenland and Antarctic Ice Sheets, Journal of Advances in Modeling Earth Systems, 13, e2021MS002 520, https://doi.org/10.1029/2021MS002520, 2021.

Smith, R. S., Bilge, T. A., Bracegirdle, T. J., Holland, P. R., Kuhlbrodt, T., Lang, C., Liddicoat, S., Mitcham, T., Mulcahy, J., Naughten, K. A., Orr, A., Palmieri, J., Payne, A. J., Rumbold, S., Stringer, M., Swaminathan, R., Taylor, S., Walton, J., and Jones, C.: Response of ice sheets, sea-ice and sea level in climate stabilisation and reversibility simulations using a state-of-the-art Earth System Model, Earth System Dynamics, 17, 475–493, https://doi.org/10.5194/esd-17-475-2026, 2026.

Spira, T., Dufour, C., Frenger, I., Richaud, B., Bennett, M. G., Bitz, C., Bracegirdle, T. J., Castellani, G., Challet, F., Paz Chidichimo, M., Cocetta, F., Diamond, R., Francis, F., Guarino, M. V., Gülk, B., Gupta, M., Haumann, F. a., Heil, P., Hoffmann-Abdi, K., Iovino, D.,

https://doi.org/10.5194/egusphere-2026-6588
Preprint. Discussion started: 22 November 2026
© Author(s) 2026. CC BY 4.0 License.

Kloecker, A., Lique, C., Martin, T., Massonnet, F., Mezzina, B., Noro, M., Oglethorpe, K., Perez, F., Silvano, A., Smith, I. J., Solomon, A. B., and Fousiya, T.: No longer polar opposites: the Arctic and the Antarctic are converging towards a seasonally dominated sea-ice regime, ESS Open Archive, https://doi.org/10.22541/essoar.176229943.38616843/v2, 2026.

Swingedouw, D., Jackson, L., Hu, A., Romanou, A., Laureanti, N. C., Weijer, W., Loriani, S., Otto-Bliesner, B., Abe-Ouchi, A., Almeida, L., Bellucci, A., Börner, R., Danabasoglu, G., Dennis, D. P., Devilliers, M., Drijfhout, S., Donges, J. F., Fröb, F., Frölicher, T. L., Gastineau, G., Goelzer, H., Guo, C., Hofmann, U., Höse, A., Jones, C., Koenigk, T., Klose, A. K., Lembo, V., Licon-Salaiz, J., Mankoff, K., Meccia, V., Melnikova, I., Mehling, O., Menviel, L., Mignot, J., Robson, J. I., Schmidt, G. A., Smith, R., Sun, Y., Trombini, I., Willeit, M., Wood, R., Wu, F., Liu, Z., and Winkelmann, R.: TIPMIP-OCEAN experimental protocol phase 1: Tipping dynamics of the AMOC, EGUsphere, https://doi.org/10.5194/egusphere-2026-1698, preprint, 2026.

West, A. E. and Blockley, E. W.: CMIP6 models overestimate sea ice melt, growth and conduction relative to ice mass balance buoy estimates, Geoscientific Model Development, 18, 3041–3064, https://doi.org/10.5194/gmd-18-3041-2025, 2025.

Williams, R. G., Ceppi, P., Roussenov, V., Katavouta, A., and Meijers, A. J.: The role of the Southern Ocean in the global climate response to carbon emissions, Philosophical transactions. Series A, Mathematical, physical, and engineering sciences, 381, 20220 062, https://doi.org/10.1098/rsta.2022.0062, 2023.

Winkelmann, R., Dennis, D. P., Donges, J. F., Loriani, S., Klose, A.-K., Abrams, J. F., Alvarez-Solas, J., Albrecht, T., Armstrong McKay, D., Bathiany, S., Blasco Navarro, J., Brovkin, V., Burke, E., Danabasoglu, G., Donner, R. V., Drüke, M., Georgievski, G., Goelzer, H., Harper, A. B., Hegerl, G., Hirota, M., Hu, A., Jackson, L. C., Jones, C., Kim, H., Koenigk, T., Lawrence, P., Lenton, T. M., Liddy, H., Licón-Saláiz, J., Menthon, M., Montoya, M., Nitzbon, J., Nowicki, S., Otto-Bliesner, B., Pausata, F., Rahmstorf, S., Ramin, K., Robinson, A., Rockström, J., Romanou, A., Sakschewski, B., Schädel, C., Sherwood, S., Smith, R. S., Steinert, N. J., Swingedouw, D., Willeit, M., Weijer, W., Wood, R., Wyser, K., and Yang, S.: The Tipping Points Modelling Intercomparison Project (TIPMIP): Assessing tipping point risks in the Earth system, EGUsphere, https://doi.org/10.5194/egusphere-2025-1899, preprint, 2025.

Wu, Y.-T., Previdi, M., Romanou, A., Lerner, P., and Polvani, L. M.: Arctic climate tipping points under delayed CO_2 emissions mitigation, Communications Earth & Environment, https://doi.org/10.1038/s43247-026-03872-7, 2026.

Xie, A., Zhu, J., Kang, S., Qin, X., Xu, B., and Wang, Y.: Polar amplification comparison among Earth's three poles under different socioeconomic scenarios from CMIP6 surface air temperature, Scientific Reports, 12, 16 548, https://doi.org/10.1038/s41598-022-21060-3, 2022.

Yang, X., Zhang, X., Agarwal, A., et al.: Polar winter processes: An under-represented research focus within the coupled Earth system, Advances in Atmospheric Sciences, https://doi.org/10.1007/s00376-026-6256-5, 2026.

Ye, K. and Messori, G.: Inter-model spread in the wintertime Arctic amplification in the CMIP6 models and the important role of internal climate variability, Global and Planetary Change, 204, 103 543, https://doi.org/https://doi.org/10.1016/j.gloplacha.2021.103543, 2021.

Yu, H., Screen, J. A., Xu, M., Hay, S., Qiu, W., and Catto, J. L.: Incomplete Arctic sea-ice recovery under CO_2 removal and its effects on the winter atmospheric circulation, Geophysical Research Letters, 52, e2024GL113 541, https://doi.org/10.1029/2024GL113541, 2025.

Zelinka, M. D., Myers, T. A., McCoy, D. T., Po-Chedley, S., Caldwell, P. M., Ceppi, P., and Taylor, K. E.: Causes of higher climate sensitivity in CMIP6 models, Geophysical Research Letters, 47, e2019GL085 782, https://doi.org/10.1029/2019GL085782, 2020.

Zhang, Y., Kong, Y., Yang, S., and Hu, X.: Asymmetric Arctic and Antarctic warming and its intermodel spread in CMIP6, Journal of Climate, 36, 8299–8310, https://doi.org/10.1175/JCLI-D-23-0118.1, 2023.

https://doi.org/10.5194/egusphere-2026-6588
Preprint. Discussion started: 22 November 2026
© Author(s) 2026. CC BY 4.0 License.



Ziehn, T., Chamberlain, M. A., Law, R. M., Lenton, A., Bodman, R. W., Dix, M., Stevens, L., Wang, Y.-P., and Srbinovsky, J.: The Australian Earth System Model: ACCESS-ESM1.5, Journal of Southern Hemisphere Earth Systems Science, 70, 193–214, https://doi.org/10.1071/ES19035, 2020.

https://doi.org/10.5194/egusphere-2026-6588
Preprint. Discussion started: 22 November 2026
© Author(s) 2026. CC BY 4.0 License.

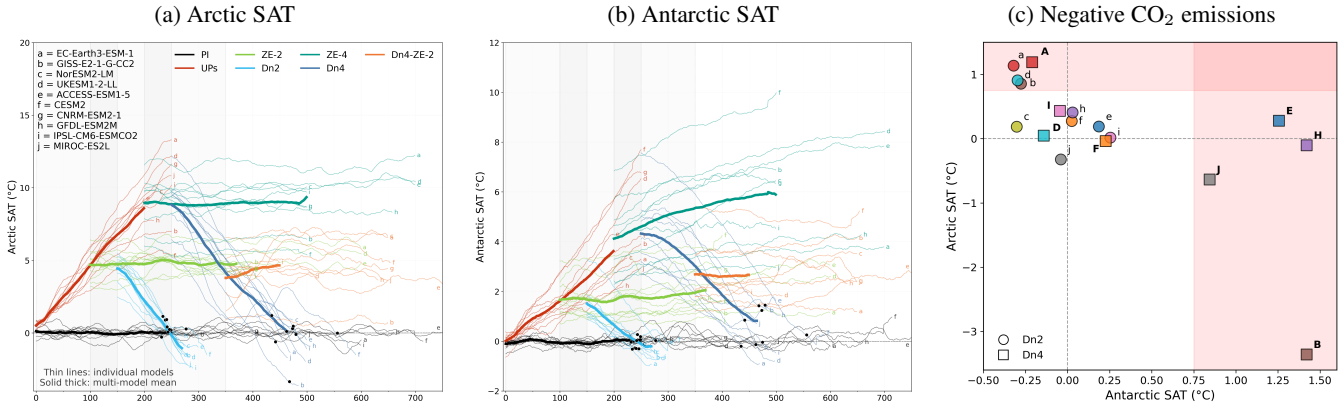

Figure 1. Overview of the TIPMIP Tier-1 temperature pathways and thermal recovery. Annual-mean surface-air-temperature (SAT) anomalies for (a) the Arctic (60–90°N) and (b) the Antarctic (90–60°S). Thin lines show individual models and thick lines the multi-model mean; colours denote PI, UPs, ZE-2, Dn2, ZE-4, Dn4 and Dn4-ZE-2 experiments (details in Table 1). Anomalies are relative to each model's 300-year PI mean (Fig. S1). Black dots mark when the 31-year smoothed GMSAT returns to the PI reference during Dn2 and Dn4. (c) Arctic and Antarctic SAT anomalies at these return points. Colours denote individual models, identified by letters a-j. Circles denote Dn2 (regular lowercase letters) and squares Dn4 (bold uppercase letters); dashed lines indicate zero SAT anomaly. Red shading highlights positive anomalies exceeding $+0.75\,^{\circ}$C, indicating delayed polar thermal recovery. NorESM2-LM does not return to the PI reference in Dn4 because the simulation is too short, while CNRM-ESM2-1 has no Dn2 or Dn4 simulations. Experiments are shifted to common nominal start years for plotting and ensemble averaging, so consecutive branches need not connect continuously because models reach the prescribed GWLs at different times.

https://doi.org/10.5194/egusphere-2026-6588
Preprint. Discussion started: 22 November 2026
© Author(s) 2026. CC BY 4.0 License.

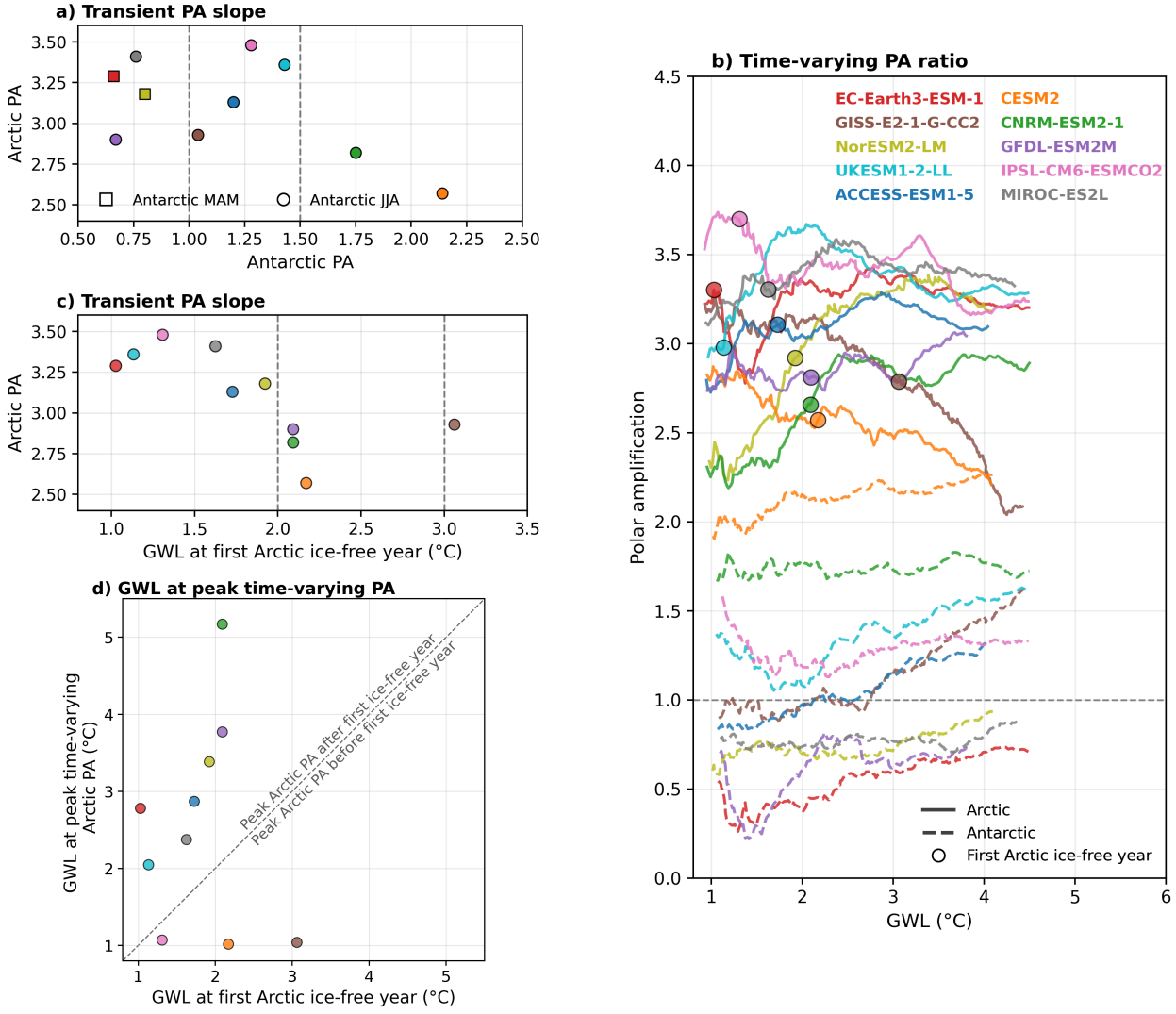

Figure 2. Polar amplification and its relationship with the first Arctic ice-free year during warming. **(a)** Maximum seasonal polar amplification (PA) during UPs. Arctic PA peaks in DJF for all models, while Antarctic PA peaks in JJA for eight models (circles) and in MAM for EC-Earth3-ESM-1 and NorESM2-LM (squares). PA is quantified from seasonal polar-to-global SAT anomaly regressions over the first 200 years of UPs (Fig. S2). **(b)** Time-varying winter PA as a function of global warming level (GWL; 31-year running-mean annual GMSAT anomaly). Arctic and Antarctic PA are calculated from 31-year running-mean DJF and JJA polar-to-global SAT anomaly ratios, respectively. Solid lines show the Arctic, dashed lines the Antarctic, and colours individual models. Filled circles mark the first Arctic ice-free summer (< 1 million km^2). **(c)** Relationship between GWL at the first Arctic ice-free year and transient winter Arctic PA, quantified from the DJF Arctic SAT–GMSAT regression slope over the first 200 years of UPs (Fig. S2a). **(d)** Comparison between GWL at the first Arctic ice-free year and GWL at peak time-varying winter Arctic PA, derived from panel (b). The dashed 1:1 line separates models in which peak Arctic PA occurs after the first ice-free year (above) from those in which it occurs before (below). PA values in panels (a)–(c) are expressed in $^\circ$C/$^\circ$C.

https://doi.org/10.5194/egusphere-2026-6588
Preprint. Discussion started: 22 November 2026
© Author(s) 2026. CC BY 4.0 License.

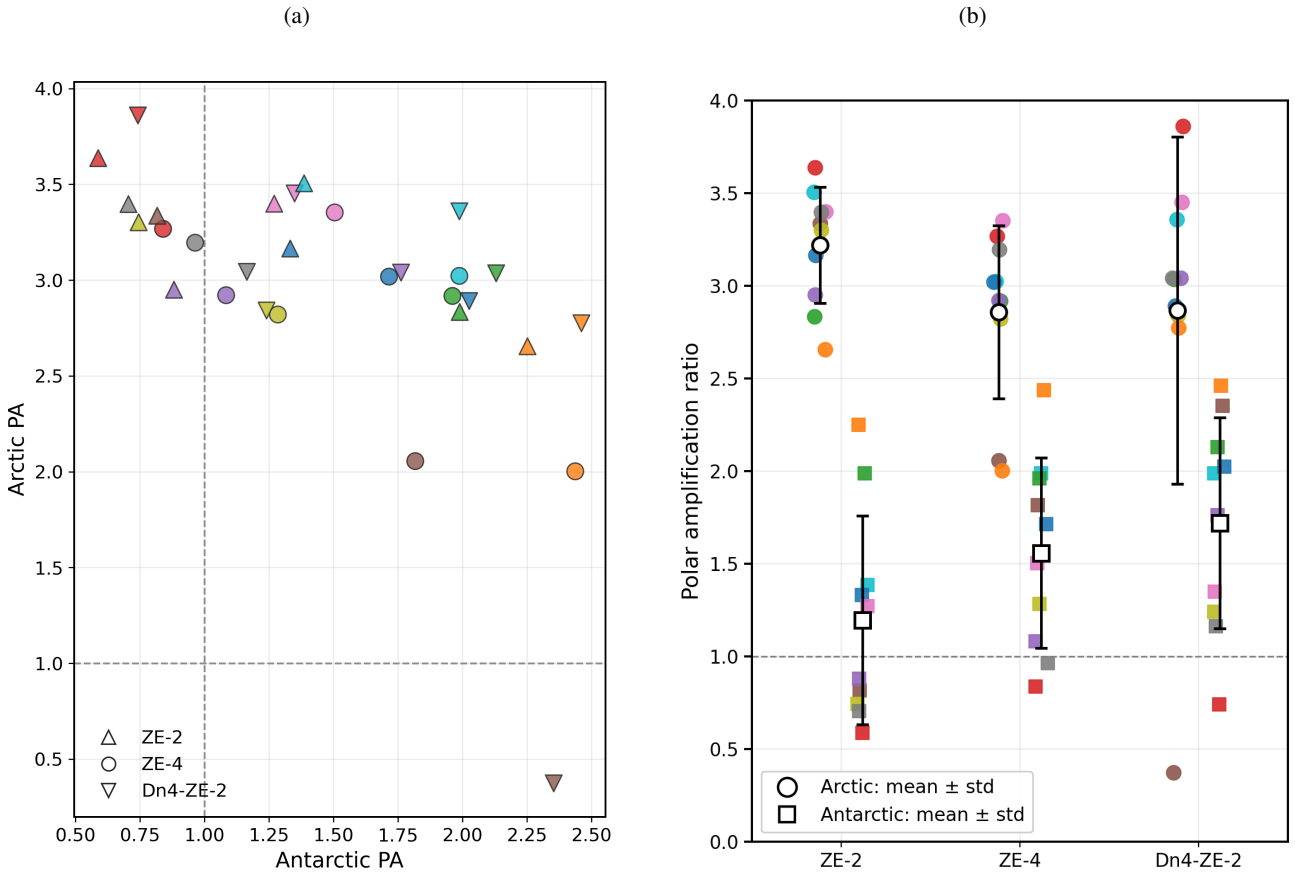

Figure 3. Winter PA under zero emissions. (a) Relationship between Arctic and Antarctic winter PA in the ZE-2, ZE-4 and Dn4-ZE-2 experiments. Arctic and Antarctic PA are calculated from DJF and JJA polar-to-global SAT anomaly ratio, respectively, using the first 300 years of each experiment. Upward triangles, circles and downward triangles denote ZE-2, ZE-4 and Dn4-ZE-2, respectively. **(b)** Model spread and multi-model mean PA for the same experiments. Circles show Arctic PA and squares Antarctic PA. Open symbols with vertical bars indicate the multi-model mean ± one standard deviation. In both panels, colours denote individual models, labelled in Fig. 2b, and dashed lines indicate a PA ratio of one.

https://doi.org/10.5194/egusphere-2026-6588
Preprint. Discussion started: 22 November 2026
© Author(s) 2026. CC BY 4.0 License.

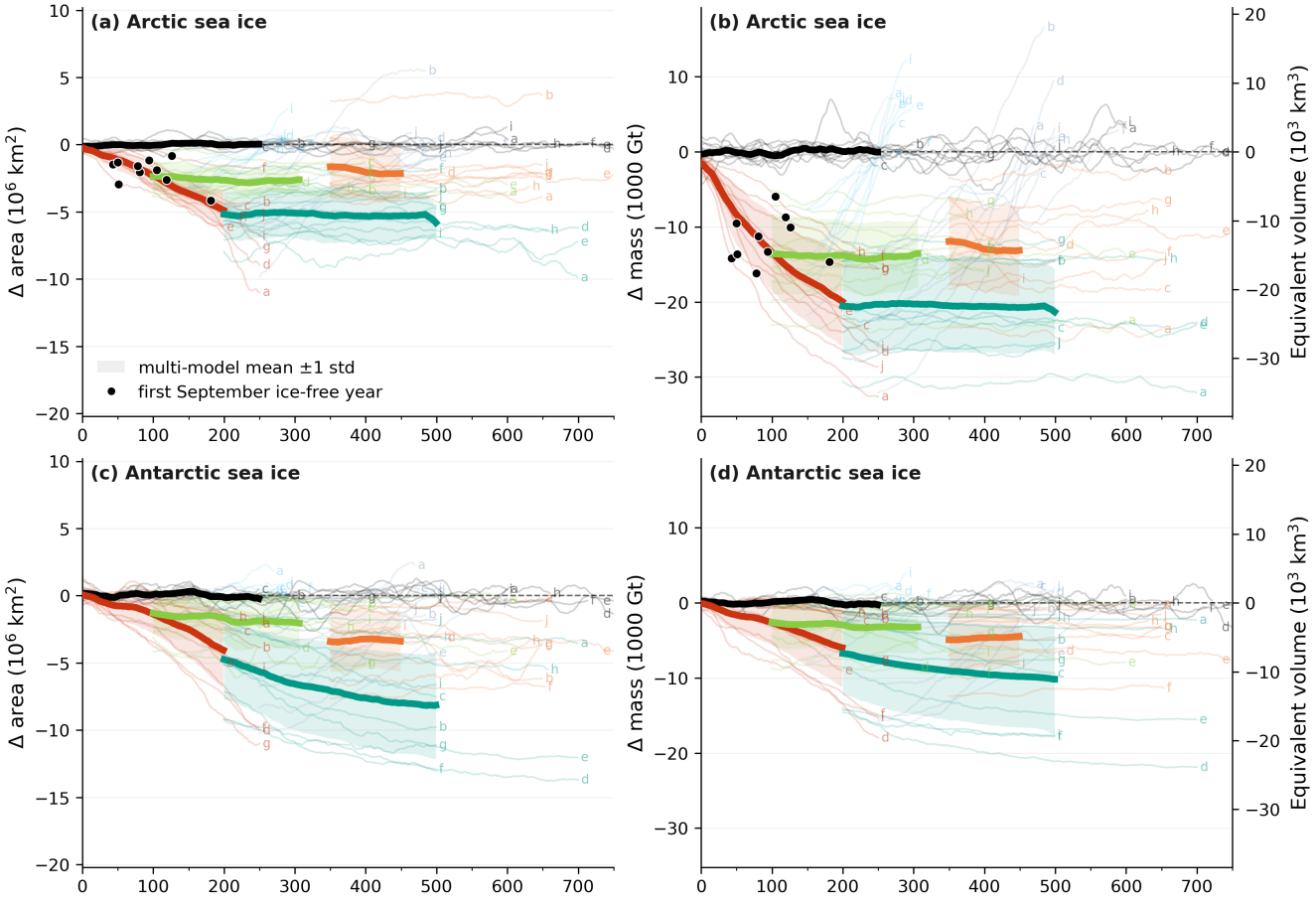

Figure 4. Multi-model winter sea ice responses across climate pathways. Winter sea ice area (**a,c**) and mass (**b,d**) anomalies in the Arctic (**a,b**) and Antarctic (**c,d**). Thin lines show individual models; thick lines show multi-model means for PI (black), UPs (red), ZE-2 (light green), ZE-4 (green) and Dn4-ZE-2 (orange), with shading indicating ±1 standard deviation for UPs and the zero-emission experiments. Dn2 and Dn4 are shown as individual trajectories only because their ensemble mean responses are analysed in Fig. 6; Dn4 is retained here to link ZE-4 to the subsequent Dn4-ZE-2 state. Colours denote the experiments, and letters a–j identify the individual models, following Figure 1. Black dots in **(a,b)** mark the first September ice-free year ($< 1 \times 10^6$ km^2). Secondary axes on the right in **(b,d)** show equivalent sea ice volume assuming a constant ice density of 917 kg m^{-3}.

https://doi.org/10.5194/egusphere-2026-6588
Preprint. Discussion started: 22 November 2026
© Author(s) 2026. CC BY 4.0 License.

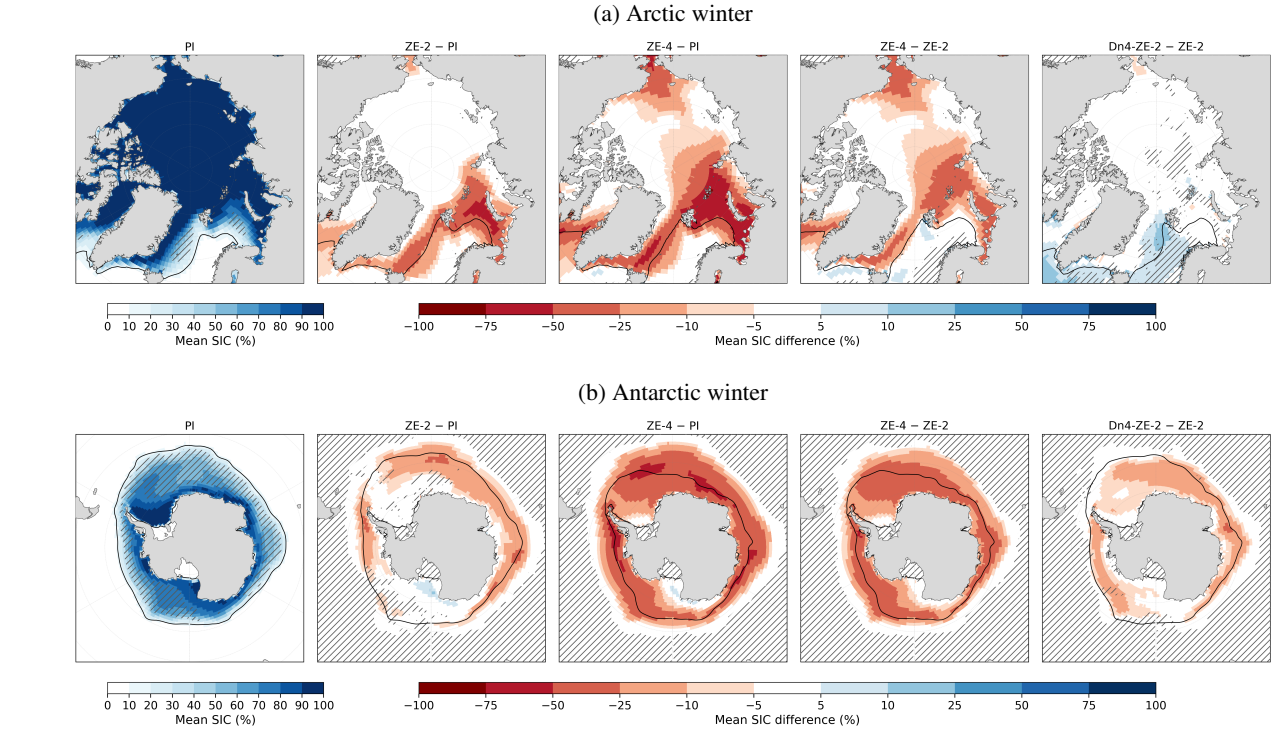

Figure 5. Mean sea ice concentration and pathway differences. The first column shows the multi-model mean PI sea ice concentration (SIC). The second and third columns show paired multi-model mean SIC differences for ZE-2 and ZE-4 relative to PI, while the fourth and fifth show ZE-4 and Dn4-ZE-2 relative to ZE-2, respectively. Rows show winter conditions for the Arctic and Antarctic. Red shading indicates lower SIC and blue shading higher SIC relative to the corresponding reference state; values between -5 and 5% are shown in white. Black contours indicate the 15% sea ice concentration edge of the corresponding multi-model mean state. Hatching in the PI panel marks regions where the inter-model ensemble standard deviation exceeds 30%. Hatching in the difference panels marks regions where fewer than six models agree on the sign of change. Model-by-model SIC temporal variability is provided in Figs. S5–S8. All states are represented by means calculated over the first 300 years of the corresponding experiment.

https://doi.org/10.5194/egusphere-2026-6588
Preprint. Discussion started: 22 November 2026
© Author(s) 2026. CC BY 4.0 License.

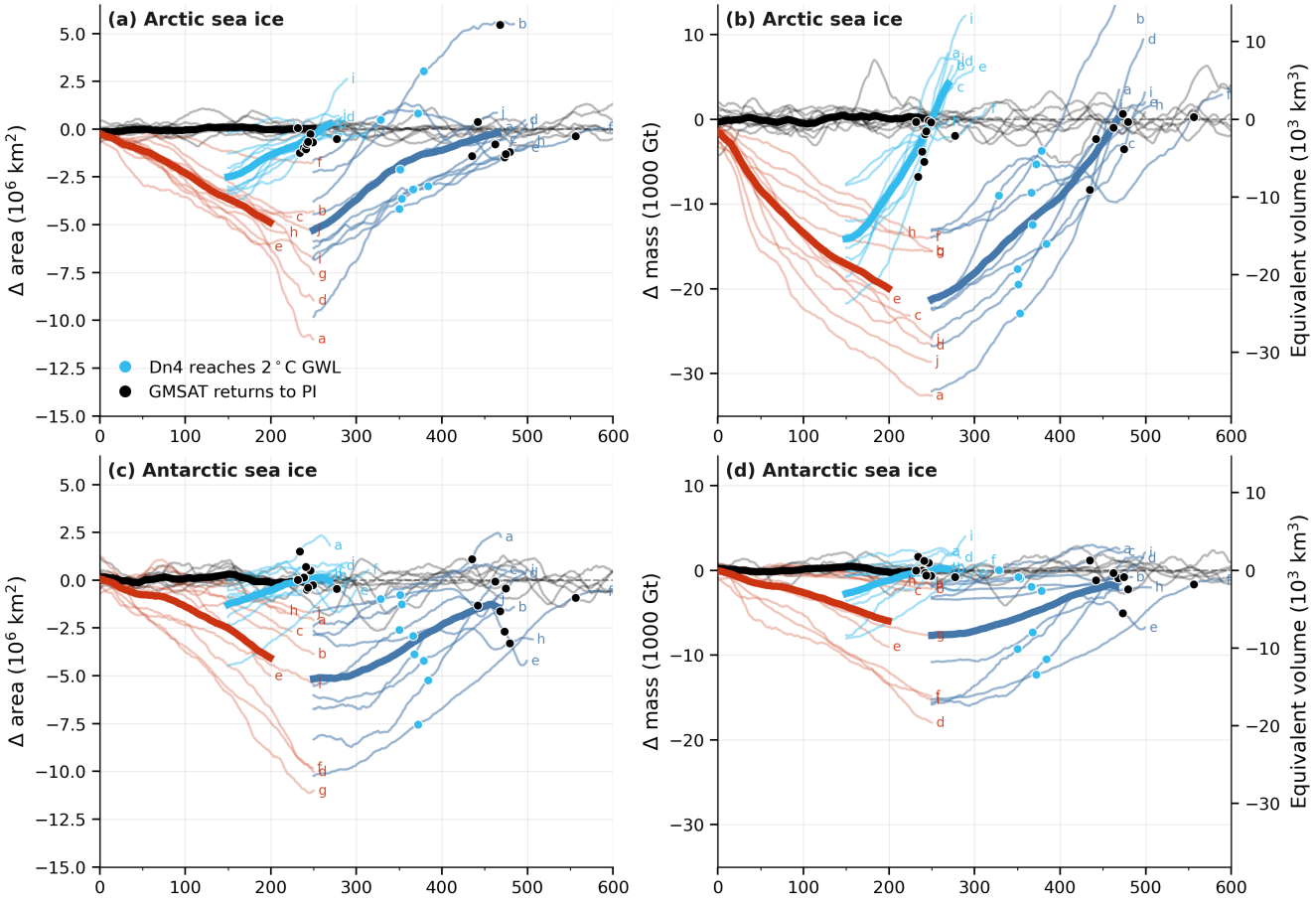

Figure 6. Winter sea ice reversibility during cooling. Sea ice area **(a,c)** and mass **(b,d)** anomalies in the Arctic **(a,b)** and Antarctic **(c,d)** during the ramp-up (UPs, red lines) and ramp-down experiments from GWL=2°C (Dn2, light blue lines) and 4°C (Dn4, dark blue lines). Thin lines show individual models and thick lines the multi-model mean; colours denote the experiments, and letters a–j identify models following Figure 1. Light-blue markers along Dn4 indicate when GMSAT returns to the 2°C GWL, while black markers indicate when Dn2 or Dn4 returns to 0°C GWL. Endpoint recovery is complete when the corresponding sea ice anomaly returns to or exceeds zero; negative values indicate incomplete recovery relative to the initial PI state. Secondary axes in **(b,d)** show equivalent sea ice volume assuming a constant ice density of 917 kg m^{-3}.

https://doi.org/10.5194/egusphere-2026-6588
Preprint. Discussion started: 22 November 2026
© Author(s) 2026. CC BY 4.0 License.

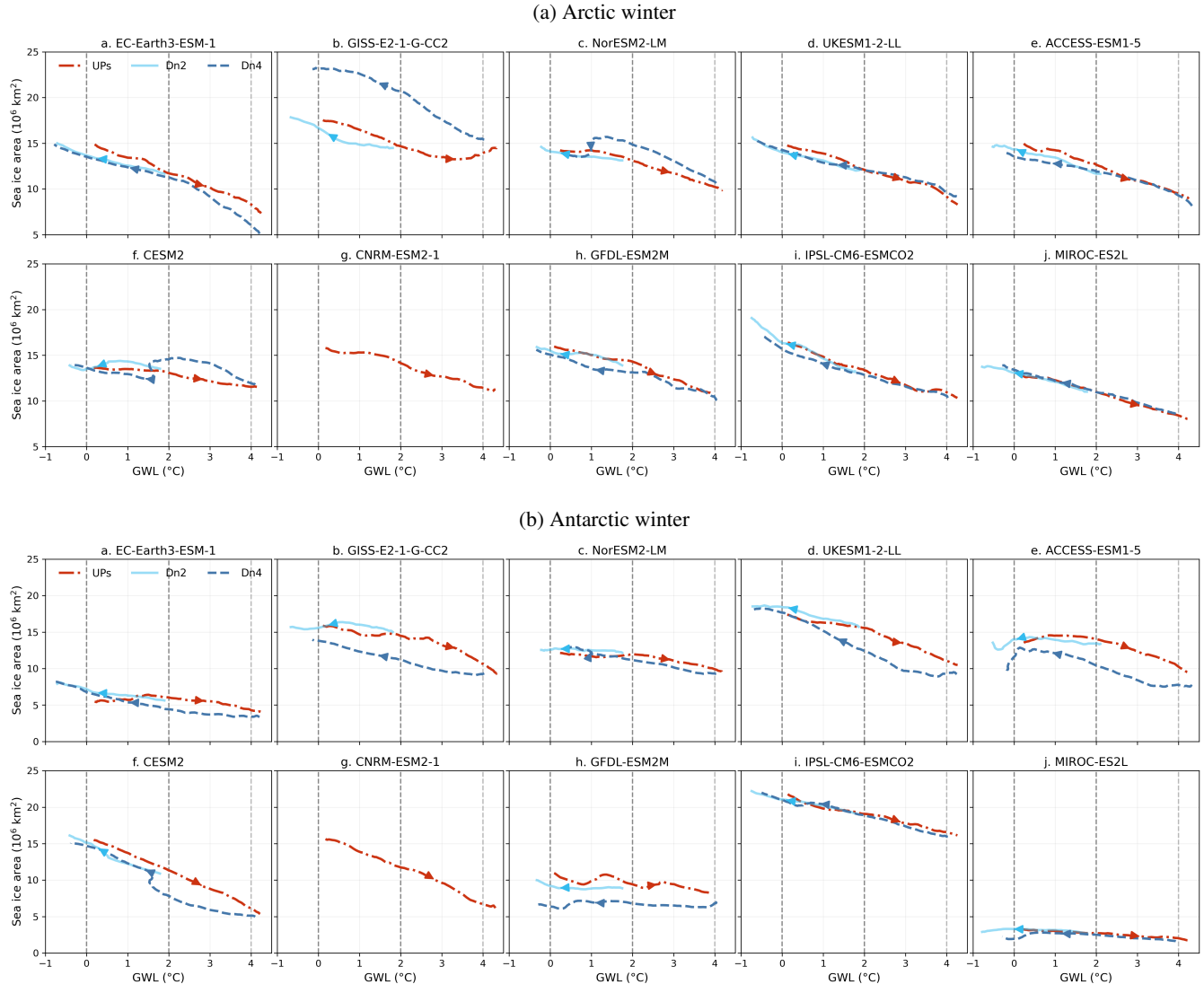

Figure 7. Reversibility of winter sea ice under ramp-up and ramp-down pathways. Arctic March and Antarctic September sea ice area are shown as functions of GWL for the ramp-up pathway (UPs) and the ramp-down pathways initiated from 2°C (Dn2) and 4°C (Dn4). Curves show 31-year running means, and arrows indicate the direction of evolution along each pathway. Vertical dashed lines mark 0, 2 and 4°C GWL. The model-specific warming and cooling branches illustrate hemispheric and inter-model differences in sea ice recovery and form the basis for the matched-GWL hysteresis diagnosed in Fig. 8.

https://doi.org/10.5194/egusphere-2026-6588
Preprint. Discussion started: 22 November 2026
© Author(s) 2026. CC BY 4.0 License.

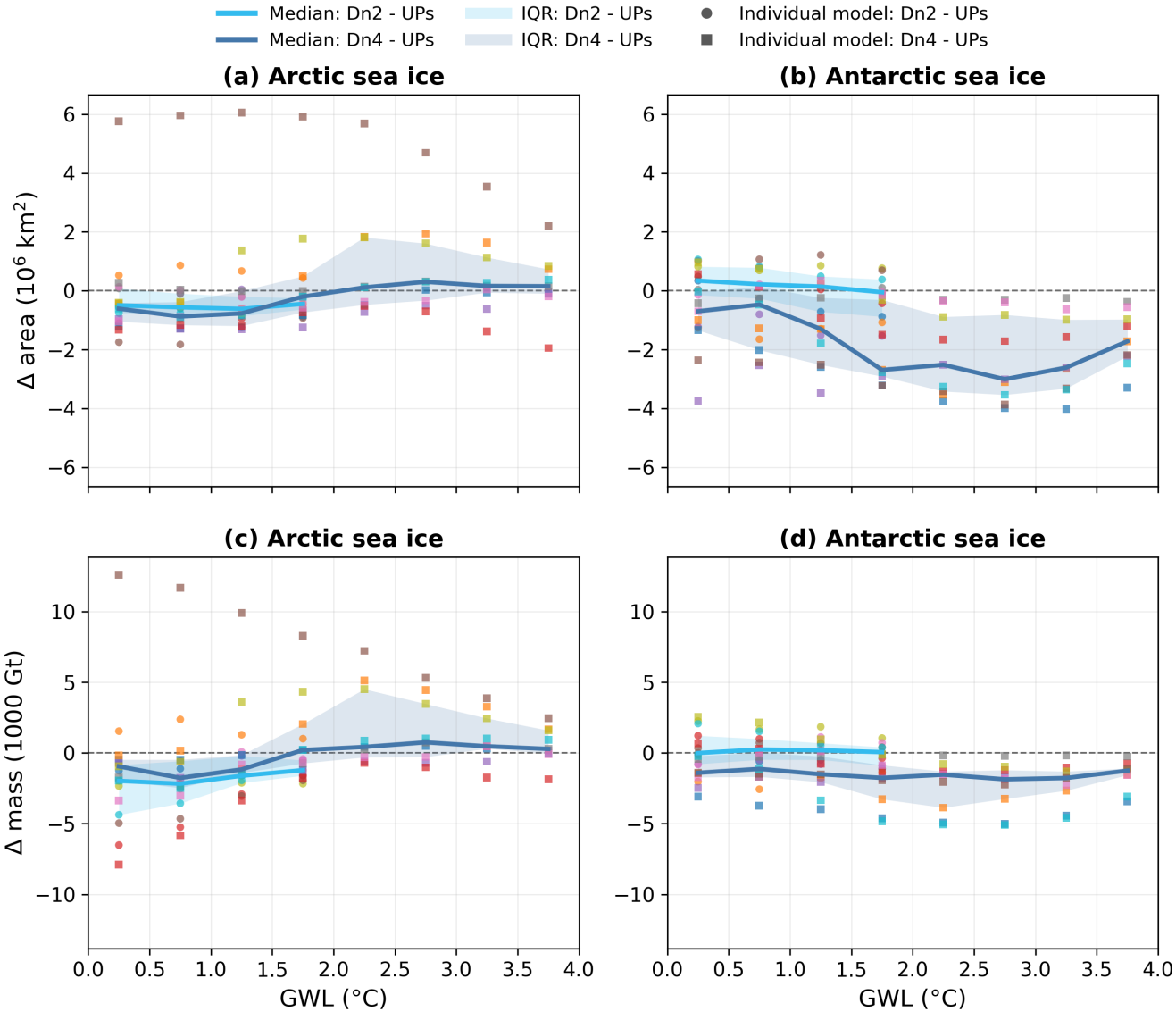

Figure 8. Matched-GWL hysteresis in sea ice area and mass. Differences in sea ice area **(a,b)** and mass **(c,d)** between ramp-down and ramp-up branches are calculated at matched GWLs. Left and right columns show the Arctic and Antarctic, respectively. Negative values indicate delayed or incomplete recovery, whereas positive values indicate over-recovery relative to the ramp-up branch at the same GWL. Individual model values are shown by coloured symbols (model colours as in Fig. 2b), with circles for Dn2–UPs and squares for Dn4–UPs. Multi-model medians (lines) and 25th–75th percentile ranges (shading) are calculated in 0.5°C GWL bins using models with paired ramp-down and ramp-up values at that warming level. The model-by-model diagnostics are shown in Figs. S10–S11.

https://doi.org/10.5194/egusphere-2026-6588
Preprint. Discussion started: 22 November 2026
© Author(s) 2026. CC BY 4.0 License.

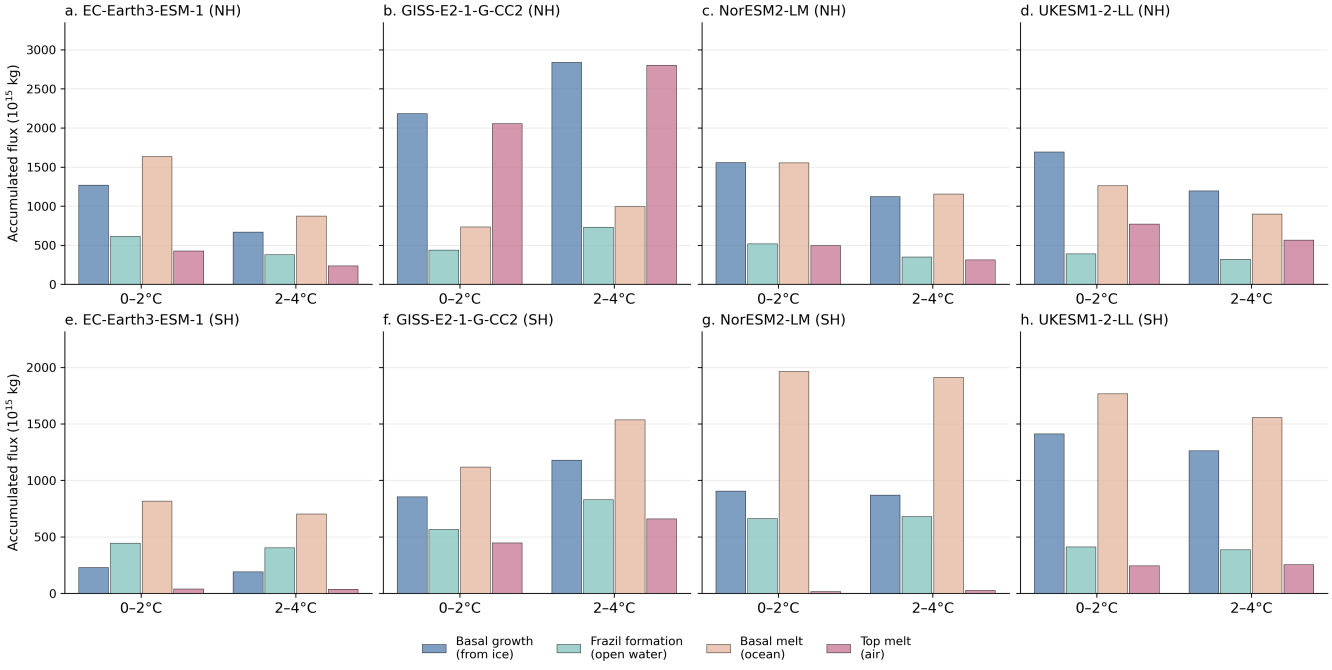

Figure 9. Integrated thermodynamic contributions to sea ice change during warming. Cumulative thermodynamic sea ice mass-budget contribution during the 0–2°C and 2–4°C stages of the UPs experiment for the Arctic (upper row) and Antarctic (lower row). Bars represent the integrated contributions from basal growth, frazil ice formation, basal melt and top melt in EC-Earth3-ESM-1, GISS-E2-1-G-CC2, NorESM2-LM and UKESM1-2-LL, respectively. Melt terms are shown as absolute values.

https://doi.org/10.5194/egusphere-2026-6588
Preprint. Discussion started: 22 November 2026
© Author(s) 2026. CC BY 4.0 License.

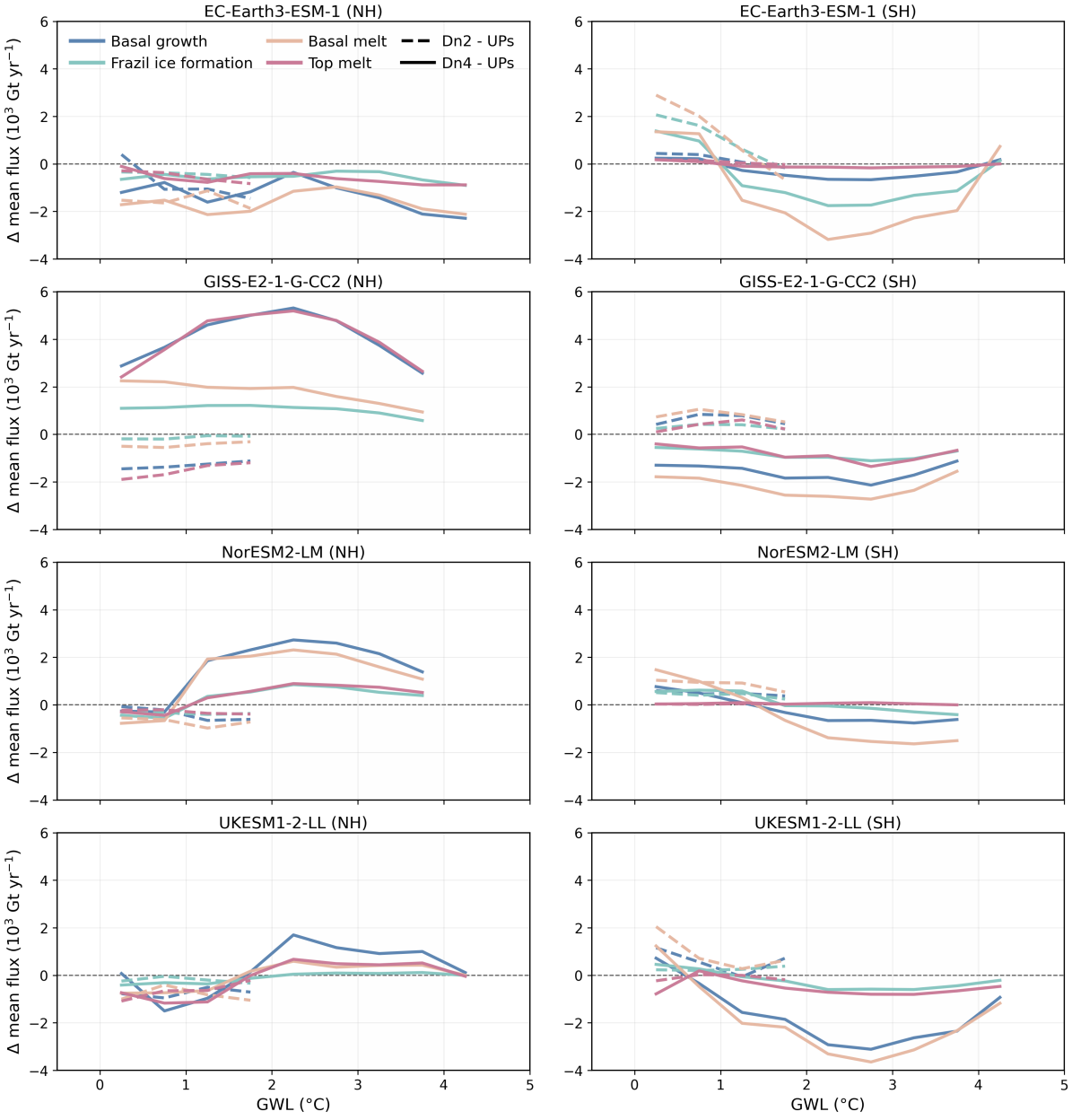

Figure 10. Thermodynamic controls on ramp-down sea ice hysteresis. Matched-GWL differences in annual-mean basal growth, frazil ice formation, basal melt, and surface melt for Dn2–UPs and Dn4–UPs. GWL matching uses 31-year-smoothed GWL, with differences calculated as ramp-down minus ramp-up. Growth and melt are expressed as positive magnitudes, so positive values indicate stronger and negative values weaker thermodynamic activity during cooling.

https://doi.org/10.5194/egusphere-2026-6588
Preprint. Discussion started: 22 November 2026
© Author(s) 2026. CC BY 4.0 License.

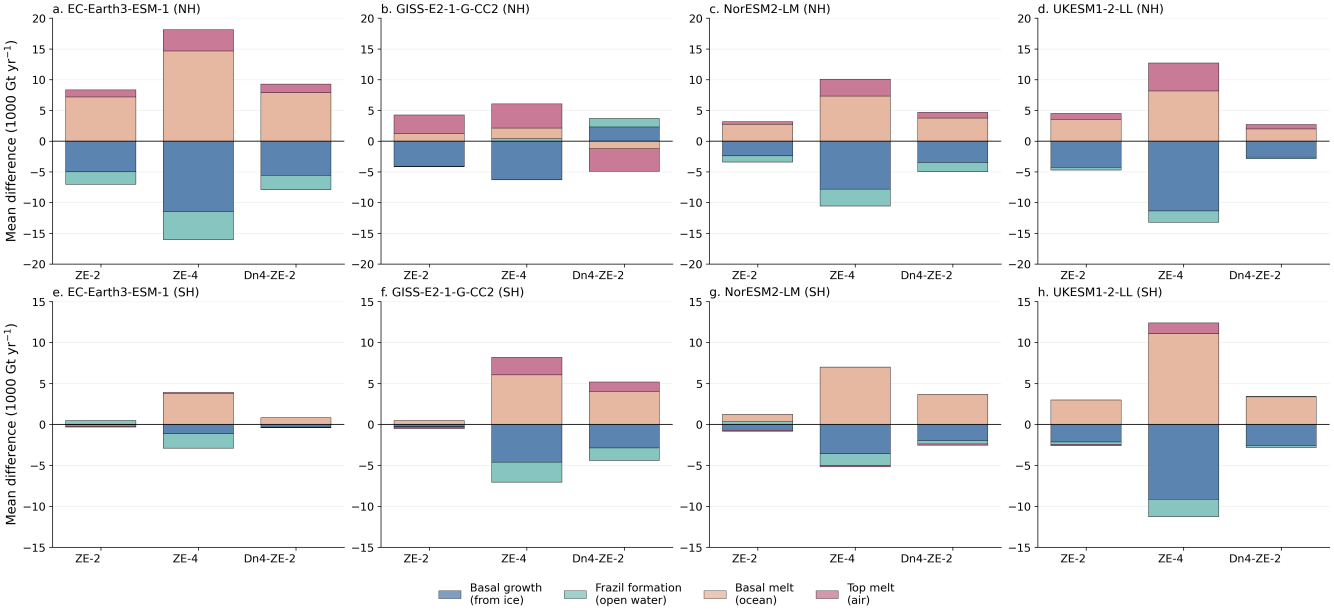

Figure 11. Thermodynamic controls on stabilised and post-overshoot sea ice states. Climatological differences in thermodynamic sea ice mass-budget terms relative to PI-control for the ZE-2, ZE-4 and Dn4-ZE-2 experiments. Panels show the Arctic and Antarctic responses for EC-Earth3-ESM-1, GISS-E2-1-G-CC2, NorESM2-LM and UKESM1-2-LL, respectively. Stacked bars denote basal growth, frazil ice formation, basal melt and top melt. For growth terms, positive and negative values indicate enhanced and reduced ice growth relative to PI-control, respectively. Because melt terms are defined as negative mass tendencies, positive melt differences indicate reduced melting, whereas negative melt differences indicate enhanced melting.

https://doi.org/10.5194/egusphere-2026-6588
Preprint. Discussion started: 22 November 2026
© Author(s) 2026. CC BY 4.0 License.

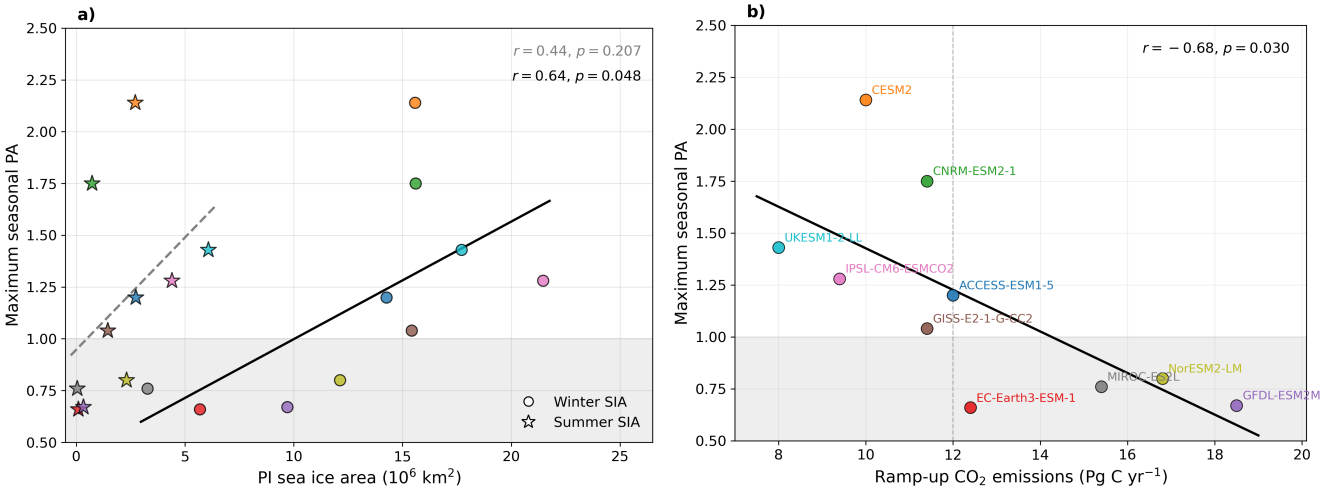

Figure 12. Antarctic amplification during warming: relationships with pre-industrial sea ice area and ramp-up CO_2-emission rate. **(a)** Maximum seasonal PA during warming, derived from Fig. S2, plotted against 300-year PI mean Antarctic sea ice area (SIA) in winter (circles; September) and summer (stars; March). **(b)** Maximum seasonal PA during warming plotted against the model-specific ramp-up CO_2 emissions prescribed to produce a global warming rate of 0.2°C per decade, based on Table 4 (Jones et al., 2026). The thin vertical dashed line marks an emission rate of 12 Pg C yr^{-1}. In both panels, colours denote individual models, and the shaded region marks PA < 1. Thick solid and dashed lines show the corresponding linear regressions, with Pearson's r and associated p values indicated.